skb.se

SKB R-23-14

ISSN 1402-3091
ID 2093360
February 2026

Upscaling rough fracture surface and hydro-mechanical experiment prediction: Modelling report of Task 10.2.2

Task 10 of SKB Task Force GWFTS – Validation approaches for groundwater flow and transport modelling with discrete features

Milan Hokr, Aleš Balvín
Technical University of Liberec

Keywords: surface roughness, fracture aperture, upscaling, prediction, validation, groundwater flow, normal stress

Abstract

The report contains the contribution of the Technical University of Liberec to Task 10.2 of the Task Force on Groundwater Flow and Transport of Solutes, focused on pragmatic validation of numerical models. It contains a task of synthetic fracture surface upscaling and simulation of hydromechanical phenomena.

The problem is based on the experiment made by Research Institutes of Sweden (RISE), from which the input and validation data was used: a granite block containing a single natural fracture was placed into an apparatus generating a hydraulic gradient in two orthogonal directions. The whole set was placed into a triaxial machine, and the force, the relative displacements of the two block parts, and the flow rate were recorded. The two fracture surfaces were represented by laser scanning data, whereby the subtraction at two corresponding vertical positions gives a raw value of aperture.

Roughness measures were evaluated for the scanned surface and from a subarea representing a fictitious drill core section. From the subarea parameters, 10 realisations of the synthetic surface were generated. The fractal parameters of the synthetic surface differ from the measured parameters which is explained by inaccurate power regression due to the limited scale range. The directional roughnesses fit well.

The hydromechanical experiment is simulated by a one-way coupled model. Its first part is the mechanical model expressing the stress-displacement relation, calculating the aperture field. It uses a set of local linear elastic problems with the contact boundary at the fracture surface: the total loading force is expressed as a sum of forces on fictitious columns above and below each surface discretisation element, provided they are in contact, depending on the raw aperture field and the applied displacement. This leads to a nonlinear stress-displacement relation. By fitting two parameters, this model can be calibrated to the measured stress-displacement curve. One of the parameters is the relative position of the two coordinate systems of laser scanning (upper and lower block piece).

The flow is calculated in a 2D horizontal projection plane, using the local cubic law (element-wise). Using the stress-dependent aperture field from the mechanical model, a stress-dependent flow is expressed. After comparison of the blind prediction for a partial load range (320 kN), higher loads were also calculated (up to 1500 kN). The model flow rate was about one order of magnitude larger than measured, but the shape of the stress-flow dependence over several orders of magnitude was quite well captured.

Sammanfattning

Denna rapport innehåller bidraget från Liberecs tekniska universitet till Task 10.2, inom SKB Task Force för grundvattenflöde och transport av lösta ämnen, som har fokus på pragmatisk validering av numeriska modeller. Rapporten behandlar en modelleringsuppgift angående uppskalning av syntetiska sprickytor och simulering av hydromekaniska fenomen.

Problemet är baserat på ett experiment som har utförts av Research Institutes of Sweden (RISE), från vilket indata och valideringsdata användes: ett granitblock som innehåller en enda naturlig spricka placerades i en apparat som genererade en hydraulisk gradient i två ortogonala riktningar. Hela uppsättningen placerades i en triaxiell maskin, varvid kraften, de relativa förskjutningarna av de två blockdelarna och vattenflödet registrerades. De två sprickytorna representerades med laserskanningsdata, varvid avståndet mellan de två motsvarande vertikala positioner ger rådata för aperturen.

Mätningar av ojämnheten utvärderades för den skannade ytan och för ett delområde som representerar en fiktiv borrkärnsektion. Från delområdesparametrarna genererades 10 realisationer av den syntetiska ytan. De fraktala parametrarna för den syntetiska ytan skiljer sig från de uppmätta parametrarna, vilket förklaras av felaktig potensregression på grund av det begränsade skalområdet. De riktningsberoende ojämnhetsvärdena stämmer väl med data.

Det hydromekaniska experimentet simuleras med en envägskopplad modell. Dess första del är den mekaniska modellen som uttrycker belastningsförskjutningsrelationen och beräknar aperturfältet. Den använder en uppsättning lokala linjära elastiska problem med kontaktgränsen vid brottytan: den totala belastningskraften uttrycks som en summa av krafter på fiktiva kolonner ovanför och under varje ytdiskretiseringselement, förutsatt att de är i kontakt, beroende på aperturfältet och den applicerade förskjutningen. Detta leder till en ickelinjär belastningsförskjutningsrelation. Genom att anpassa två parametrar kan denna modell kalibreras till den uppmätta belastningsförskjutningskurvan. En av parametrarna är den relativa positionen för de två koordinatsystemen för laserskanningen av det övre och nedre blockstycket.

Flödet beräknades i ett 2D horisontellt projektionsplan med hjälp av den lokala kubiska lagen (elementvis). Med hjälp av det belastningsberoende aperturfältet från den mekaniska modellen uttrycks ett belastningsberoende flöde. Efter en jämförelse av den ”blinda” prediktionen, när det experimentella resultatet är okänt, för ett partiellt lastområde (det vill säga 320 kN) med det experimentella resultatet, beräknades även flödet för högre belastningar (upp till 1500 kN). Modellflödet var ungefär en storleksordning större än det uppmätta, men formen på belastningsflödesberoendet över flera storleksordningar fångades ganska väl.

Content

1 Introduction

The idea of Task 10 is to develop a methodology that improves confidence in models when the validation in a strict sense is not possible. The detailed context is defined by the task description (Bruines, unpublished, and will be denoted solely Task Description in the following of this report[1]). Generic ideas, a literature review, and a formulation of a particular procedure were addressed in Subtask 10.1. This involved selected experts and resulted in a paper (Lanyon et al. 2021) and a detailed report (Lanyon et al. 2024).

Subtask 10.2. focuses on the participation of individual modelling teams in a prescribed problem that serves as a framework for exercising prediction and validation. The particular topic is the single fracture scale problem, which is part of the broader needs to predict flow and solute transport phenomena under various conditions. The challenge arises from having limited data from site investigations and laboratory measurements. Subtask 10.2. consists of two steps: 10.2.1 and 10.2.2. The first step introduced participants to the structure of the data from an excavated granite block containing a single natural fracture. It also covered roughness metrics, synthetic surface generation, and the use of data in numerical flow and transport models. The results from all teams were compiled into a single report (Finsterle et al. 2024). The current report focuses on the second step, Task 10.2.2.

Participation of authors in Task 10 is covered by the Czech national waste management organization SÚRAO. The Czech deep geological repository (DGR) concept considers crystalline host rock where the prediction of rock fracture transmissivities will be one of the essential issues. Therefore, the objective of Task 10.2—to extrapolate the drillcore-scale fracture surface and aperture observations to the larger scale of the whole fracture plane—is directly relevant to SÚRAO's safety case.

---

[1] Bruines, P. SKB Task Force on Modelling of Groundwater Flow and Transport of Solutes: Description of Task 10.2. SKB R-23-10, Svensk Kärnbränslehantering AB, Stockholm, Sweden. Unpublished.

2 Description and objectives of Task 10.2.2

2.1 Objectives of Task 10.2.2

According to the task assignment document (Task Description), the objectives are:

- Prediction and validation of the upscaled fracture geometry from borehole-sized fracture geometry and/or fracture trace geometry.
- Prediction and validation of flow across a fracture at different normal stresses.
- Support of the development and demonstration of the pragmatic validation workflow at the single fracture scale.

The actual objectives considered for the presented work were the same in the generic sense, but in several cases the detailed extent could be reduced. In particular:

- Demonstrate the use of the fractal surface roughness model for fracture geometry upscaling. Verify the upscaled surface using various other surface roughness measures and against a measured larger-scale sample.
- Capture the coupled hydro-mechanical behaviour of a single fracture. Define the problem so that part of the data could be used for model calibration and part of the data for validation, comparing the prediction against the remaining part of the data.

2.2 Limitation of Task 10.2.2

The respective section of the Task Description discusses the limitation related to representativeness of the studied fracture to other fractures in the rock mass, depending on geological genesis.

Particular limitations in this work result from not fully following the assignment, due to available software tools and limited work capacity. In particular, the prediction (synthetic generation) of fracture surfaces was separated from the hydro-mechanical modelling – the hydromechanical model is evaluated with the deterministic measured sample fracture surface, not with the synthetic generated and upscaled surface. No synthetic aperture field (correlated surfaces) is generated.

The roughness measure evaluations are limited by the scale range of the used data – spatial resolution of the laser scanning from the bottom and the sample sizes from the top. The fractal model used for upscaling may not be fully valid.

The physics in the hydro-mechanical model is partly simplified: The stress and deformation are solved as contacts of local "columns" that are independent of each other. The local cubic law is applied for the flow calculation.

Next, the validation process is weakened when not all provided data was used (or not fully analysed in relation to the model) – see comments in the next section on data description. Moreover, some of the data contain experimental artefacts, which are hard to detect and exclude, so a simplified form or postprocessing of such data is used for either model input or validation (e.g. the displacement as an average of four LVDTs, cropping the fracture sample's borders).

2.3 Data description

In this section, the data provided as part of the task assignment is described. We focus on the actual use of the data for the modelling (input, calibration, validation). To precisely distinguish between the provided raw data and the ones actually used, we discuss the introductory data processing in separate subsections – defining model inputs from the measured raw data and the conceptual interpretation for modelling decisions, which are easier to explain in the context of data rather than in the context of the modelling procedure described in Section 3.

2.3.1 Experiment design

The data is all related to the granite block with a single natural fracture and to the hydromechanical experiment of flow through the fracture loaded by normal force. The block has dimensions of 200 × 200 × 250 mm (length × width × height), the fracture is oriented horizontally approximately in the middle of the height. A frame is attached to the upper and lower blocks and four LVDT sensors connect the corners of the frames to capture opening/closing of the fracture. The whole set is placed into a triaxial test apparatus to provide the normal loading force (see the Task description) for details and graphics).

Water inlet/outlet can be attached to any of the sides, covering most of the fracture trace, assuming a uniform gradient. Hydraulic pressure is controlled by varying the height of overflow, and the flow rate is determined by weighting the collected outlet water. Tap water was used. The two applied gradient directions are illustrated in Figure 2-1.

The actual sequence of changing load (increasing/decreasing), pressure gradient direction, and block manipulation was recorded (see details below).

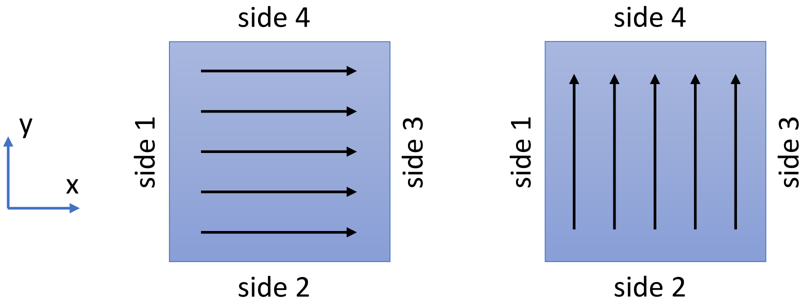

Figure 2-1. *Scheme of the hydraulic fracture measurement: two pressure gradients are denoted as 1-3 and 2-4; in each case there is one inlet side, one outlet side and two sides impermeable.*

2.3.2 Fracture surface

After the first series of hydromechanical tests, the block was opened to access each of the fracture surfaces, to measure the surface geometry by laser scanning using a handheld laser scanner with a precision of 0.035 mm and the resolution of 0.1–0.2 mm. The laser scan data of the fracture surfaces was obtained in two formats – ASCII files (point cloud with X, Y, Z coordinates) and STL files (triangulation). Since the latter covered all rock block sides (the external sides, not just the fracture surface, see Figure 2-2) and it would be difficult to detect and extract the sub-set of data which belongs to the fracture itself, the ASCII files were used for creation of a regular grid in Surfer software (Golden Software 2023).

Next, subsets of these data corresponding to circular domains representing intersections of the fracture with a hypothetical borehole (i.e. representing the observable fracture surface in the drill-core) were provided, already in the STL format, but an alternative choice of the borehole-scale surfaces was used for technical reasons as described below.

Data preprocessing

The grid resolution was set to 0.1 mm and kriging was used as the interpolation method. The choice fits the documented resolution of the source data and keeps the resulting data reasonably large. To exclude potential irregularities at the edges (see Figure 2-2), the area was cropped by 5 mm from each side. The actual area of 190 x 190 mm was input into the calculations, with necessary adjustments of other model inputs and outputs. But the report text and the presented values are denoted as being from the original dimension of 200 mm or from the “whole block”, to emphasize the contrast to the smaller-scale data.

Next, the grids were converted to STL format, which is the required input format of the free software "Surface Roughness Calculator" (SRC) (Magsipoc et al. 2020). The export from the grid to STL was available in Surfer version 23. The conversion is also built-in in SRC, but we detected a bug explained below in Section 3.1.2. The triangles of STL are constructed by splitting each grid square at its diagonal. An example comparison of the original STL surface data and the STL obtained from the gridded data is shown in Figure 2-3.

The provided STL files of the circular subsets (boreholes) could not be used because, according to our experience, SRC does not analyse areas other than rectangular correctly. So, as an alternative way of representing the "borehole" data, we used a square area for which the borehole is the circumscribed circle. To capture eventual sensitivity of the results on the data processing, we used several options for the square size and gridding resolution:

- 39.5 mm, 38 mm, and 30 mm squares, each centred with respect to the whole surface, with some variants for the smaller placed at the sides of the largest square
- 0.1 mm, 0.05 mm, 0.025 mm grid resolution

The processing of data is the same as for the whole block described in the above two paragraphs.

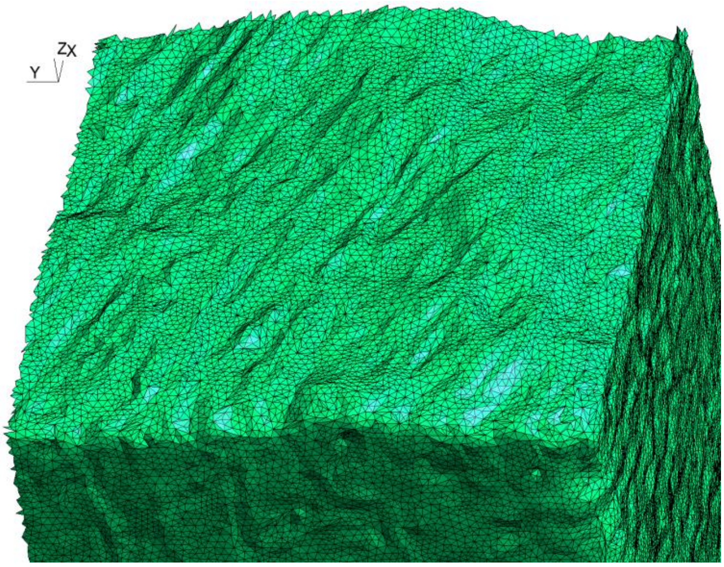

Figure 2-2. *A crop from the source STL files with the fracture surface on the top and the free block sides (yz and xz planes). Approximately 10 mm × 10 mm area is shown in the fracture plane.*

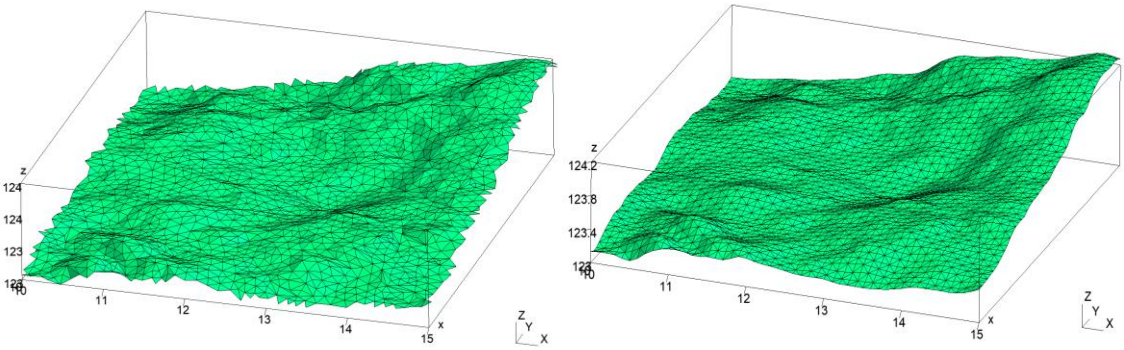

Figure 2-3. *Comparison of source (left) and gridded (right) fracture surface data for a sample area 5 mm × 5 mm (all coordinates in mm).*

2.3.3 Stress-deformation LVDT measurement

For mechanical behaviour, data of the fracture normal compression stiffness is provided as part of the hydromechanical test. The normal force and the four displacements of the LVDT sensors are the main data to be used. We distinguish five subsets of the data: four represent the data supporting the prediction model, from tests on the unopened block, for each hydraulic gradient (1-3 and 2-4) the loading and unloading stages. The fifth subset represents the validation data, disclosed after the prediction model was set up, and comprises several loading/unloading stages on the opened and resealed block, including application of higher load force than applied on the unopened block (presented later together with the prediction-outcome exercise results).

In Figure 2-4, detailed data of the loading stage with the 2-4 hydraulic gradient is analysed. During the early loading steps, the behaviour is irregular, with a possible relative rotation of the upper and lower blocks (plotted as change of slope – regression factors at *x* and *y*). Later, the deformation evolves more uniformly.

Data preprocessing

The average value of the four individual sensors captures the main trend representing the fracture normal stiffness; only the average is used in the further processing to keep the problem not overly complicated. Another reason for applying this simplification (assuming no rotation) is that the four sensors do not evolve as four points on a rigid plane – the distance of the fourth point from the plane of the other three evolves from 0.003 mm to 0.05 mm, i.e., on the same order of magnitude as the displacements (data not presented).

Next, the four experimental stages are evaluated, with the use of the sensor averages only (Figure 2-5). There is significant hysteresis of the loading and unloading stages. The two hydraulic gradients have similar patterns but differ in the overall shift and slightly in the slope (effective stiffness). We consider the shift as an effect of a manipulation and do not include it in the evaluation. Also, having a non-linear elastic model, we do not take into account the hysteresis (nor any other plasticity and damage effect). For the purpose of model calibration, we only extract a single value of the normal stiffness from this set of the experimental data, corresponding to the 2-4 loading stage (Figure 2-5 grey line).

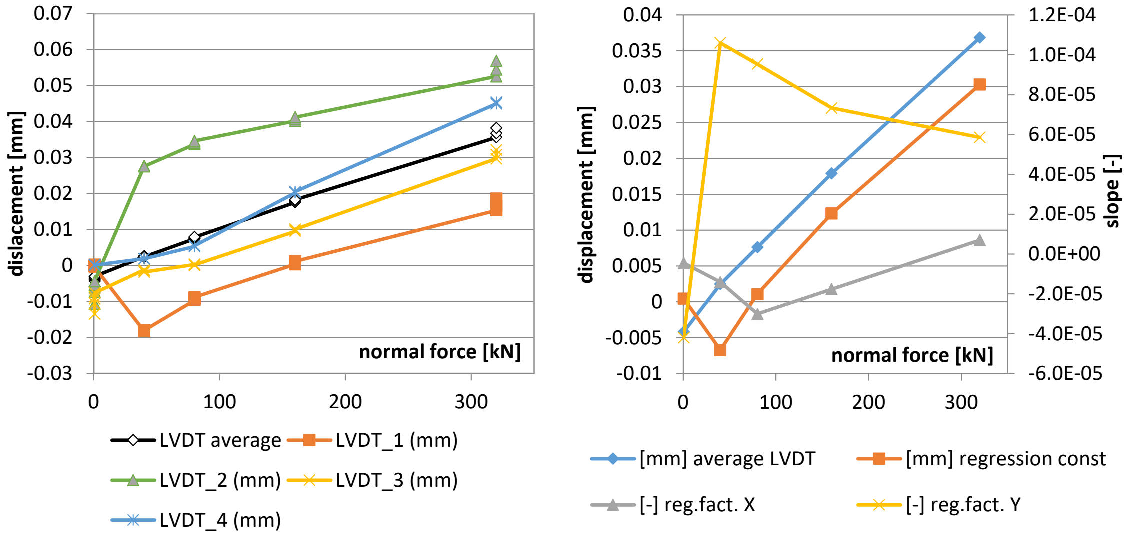

Figure 2-4. *(Left) Record of individual LVDT sensors during loading stage of the 2-4 gradient direction test, together with their average. (Right) Comparison of the average of the LVDTs with data describing a movement of the regression plane through the four LVDT positions during the loading steps (constant and the two linear factors).*

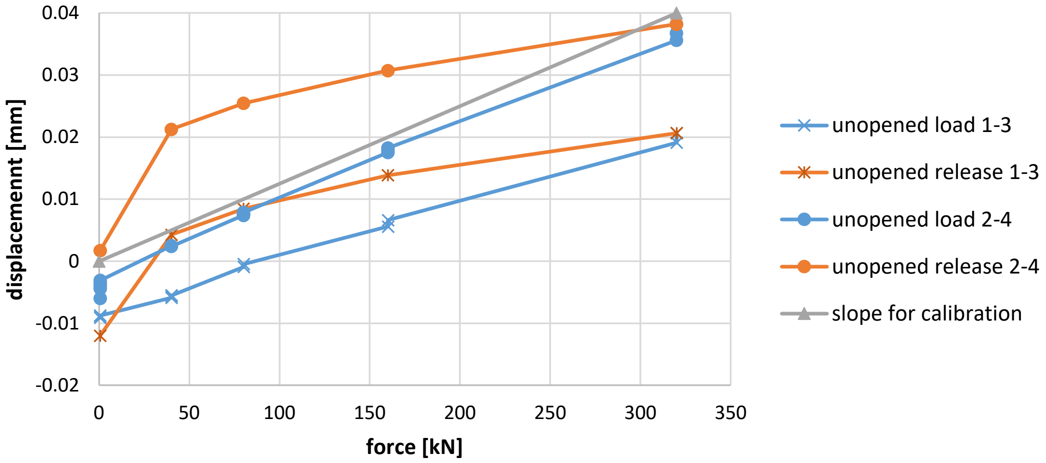

Figure 2-5. *LVDT data from four experiment stages, as averages of the individual sensors. The grey line represents the chosen stiffness for the mechanical model calibration.*

Next, rock matrix elastic and strength properties were measured on the core samples. The laboratory measurements yielded Young's modulus values in the range 71.7–74.6 GPa; a representative value of 70 GPa was adopted as a model input to account for potential scale effects and material heterogeneity at the block scale.

2.3.4 Flow rate measurement

The flow rate measurement was obtained as part of the hydromechanical test, together with the LVDT measurement above, sorted within one table, in separate columns. Based on the prediction and validation task concept, this data was disclosed later, after calculating the model based on remaining input data, as the blind prediction exercise. Preliminary information about the actual, "very small" flow rate became available in early discussions of the task, so this soft information (with a range of about one or two orders of magnitude) could be considered during model set-up and the predictions. In particular, calibration of the applied block position adjustment (although made based on the stress-displacement measurement) could be adapted to make sure the aperture and consequently the transmissivity corresponds to the observed flow behaviour.

In each gradient direction, 1-3 (along x axis) and 2-4 (along y axis) and for each loading step of normal force, input and output pressures, flow rates, and temperature-dependent densities and viscosities are recorded.

Data preprocessing

In some of the load steps, more flow data is recorded, with different pressure gradients. These cases are also visible as multiple points (discontinuities) on the force-displacement plots (Figure 2-4, Figure 2-5). Because only the one-way coupling is considered in the model (flow is affected by stress/deformation, but the effective stress is not affected by water pressure changes) and a linear flow model is used, the effect of the pressure gradient is not evaluated, considering all pressure conditions as qualitatively equivalent, just with linear scaling in the flow model. From the stress-displacement plots, minor effects of hydraulic pressure on the mechanical deformation can be interpreted (the differences between the pressure gradient cases are much smaller than differences between the load cases in Figure 2-4). In contrast, the differences between the pressure gradient cases were visually larger on the stress–flow rate plots, from the data disclosed after the prediction was finished (Figure 4-5). Unfortunately, these visualisations alone do not explain the reason of the deviation from the proportionality of flow rate and pressure gradient. For the purpose of later model-measurement comparison, the flow rates were normalized to unit pressure difference (1 bar) – so the non-proportionality is shown as a group of different flow rates for a particular load step (this is shown together with the model comparison in Section 4.2).

2.3.5 Other

Additionally, we briefly list other data which was provided together with the task assignment but was not used for the model and analysis – for either reason of available methodology, software tools, or work capacity:

- Photographs of the fracture traces on the block sides, with a ruler for scale and the reported bitmap resolution could in principle be used to obtain an estimate of aperture at the side of the fracture. This could be an additional argument to reduce the fracture aperture from the raw calculation of the upper/lower coordinate subtraction (described below) by shifting the coordinate system. Also, the pictures could indirectly support for the decision of horizontal cropping of the fracture geometry data – seeing the irregular edges with potentially open space not in accordance with disclosed knowledge of "small flow rate".
- Geometry of the assembled block outer surface.
- Pressure films (they were visually compared with the obtained aperture fields but no numerical inputs or conceptual contributions to modelling were made).
- Photos of debris during the fracture opening – they prove the laser scan surface does not represent the natural state during the preceding stages of the hydromechanical experiments.
- Tracer staining test.

2.4 Pragmatic validation

The concept and detailed explanation of pragmatic validation are given in Lanyon et al. (2021) and Lanyon et al. (2024). The suggested application to this task is formulated into these steps according to the Task Description:

1. Definition of the model purpose: Specify the intended purpose of the model is a crucial aspect of model-evaluation, as the model-purpose helps determine the benchmark and standards for critical evaluation.
    a. The purpose was in a narrower focus than the whole Task 10.2.2 definition. Two independent exercises were actually solved, so two points of the model purpose are given as the objectives in 2.1
2. Domain of model applicability and prediction, including limits of applicability identified in the Pragmatic Validation exercise and limitations required to make the exercise possible.
    a. There were several simplifications and assumptions applied as given in the respective sections. This means that the applicability quite reduced, i.e., appropriate for the modelling exercise in this report rather than for general evaluation of the rock fractures in the DGR safety assessment.
3. Determination of critical aspects: Identify aspects of modelling that are specific to the intended use and which therefore require validation.
    a. The assumptions and simplifications which were found critical are listed in 3.1.3
4. Definition of performance measures and criteria: Discussion of the basis for performance measures and acceptance criteria specific to the model purpose and conceptual/numerical models used.
    a. The performance measures and criteria were, in a general sense, contained in the Task definition. They are linked with the actually measured data. Their particular use depends on the type of the numerical model. For the fracture surface upscaling, we used the single surface roughness measures, but not the aperture field (as the artificial surfaces were not generated in correlated couples). For the hydromechanical experiments, the predicted and measured flow rates were compared, and the range of the stresses was extended.
5. Conceptual assumptions being tested by the Pragmatic Validation exercise (e.g., DFN geometric models, plate flow, correlations between geometric/hydraulic/geomechanical properties).

6. Approaches for derivation of numerical parameters being tested by the Pragmatic Validation exercise (e.g., boundary conditions, material properties, fracture geometries, microstructural models).
    a. For the fracture roughness analysis, different surface data resolution is tested and the dependence on surface subset choice.
    b. For the hydromechanical problem, the main part of parameters is tested (calibrated) against the mechanical measurement only (purely mechanical model).
7. Understanding of the scope and limitations of experimental data and theoretical concepts being used to support modelling and performance measures. The accuracy of both the model output and data must be sufficiently high that they are discriminative in the evaluation of the acceptance criteria.
    a. This was hard to achieve in these exercises. They were some hypotheses why the upscale fracture roughness did not fully fit the measured one. The mechanical model was known it eventually cannot capture the real behaviour due to simplification of the physics.
8. Sensitivity and uncertainty analysis of influential factors. Provide details of the sensitivity and uncertainty analyses necessary to support a determination of which factors are most critical to Pragmatic Validation.
    a. This was not achieved due to limited work capacity.
9. Prediction-outcome exercises: Details of modelling carried out to support Prediction-Outcome exercises, including identification of uncertainties in predictions due to underlying data, and also uncertainties due to underlying assumptions and simplifications.
    a. This was made, together with the next point, as the main part of the work. Development of the model suitable for the supporting measured data, calculation of variants, understanding the relation of the model to the real physical behaviour.
10. Model evaluation, documentation and model audit: Qualitative and quantitative assessment of model performance measures as compared to the prediction-outcome exercise models.
    a. Focus was made on discussing the differences between the model prediction and the measurement, finding possible links to the applied simplifications.
11. Pragmatic validation statements: Explicitly state what level of pragmatic validation was achieved by the exercise as conducted, how this exercise could be improved, and what might be required to achieve validation sufficient for the model purpose.
    a. This is a subject of the final discussion, but limited to the applied modelling approaches covering only a part of the whole Task 10.2.2

Some of the points are not actually subject of this report but cover the participation of the evaluator and other TF participants.

3 Modelling and methodology

3.1 Modelling tasks

3.1.1 Model purpose

The ultimate purpose could be a prediction of flow and transport in any fracture, depending on its subarea on a drill core and on an estimate of in-situ mechanical load and its changes due to excavations. In practice, this does not mean that if such models were available, every fracture under every mechanical condition would be analysed in such model, contributing to the solute transport in the repository safety assessment. In the context of TF GWFTS, the model purpose is to provide an exercise to go through the steps of pragmatic validation. In the context of real repository safety assessment, the purpose is to show that the individual fractures can be predicted at this scale level and to provide a methodology for upscaling to the type of model actually used for a safety assessment.

The particular purposes are:

- Determine the roughness of larger scale surfaces based on a smaller subarea of the surface
- Determine the aperture field from two scanned surfaces
- Evaluate the dependence of fracture flow rate on normal stress on a fracture
- Find which data is important to determine the relevant model parameters

3.1.2 Model description

In this section, the conceptual ideas, processes, equations, and practical application of the models, data adjustments, and calculation procedures are presented in non-numbered subsections according to the individual topics. The "model" term is used in a rather generic sense, including the numerical solution of the governing equations, representation of features/phenomena by derived quantities, procedures to obtain descriptive data, etc. The software used for a particular task is also mentioned.

Roughness measures

The surface roughness analysis and the synthetic surface generation are based on the various roughness measures defined below. The algorithms for the roughness measures calculation are implemented in the SRC software. For a full explanation, we refer the reader to its documentation, the review paper (Magsipoc et al. 2020) and references therein. The following roughness measures are used in this work:

- Root-mean-square (RMS) of the surface vertical position, $R_q = \sqrt{\frac{1}{S}\int_S (z - z_{av})^2}$, where *z(x,y)* is the surface function, z_{av} is its average, *S* is the area (in SRC, it is separately evaluated for line profiles only, for *z(x)* and the length instead of the area, but the area case is also a part of the fractal analysis below). De-trended surface (a rotation to the horizontal regression plane) should be considered as input.
- Roughness metric (directional-dependent) $\theta_{max}{}^*/(C+1)$, where $\theta_{max}{}^*$ is the maximum inclination angle and *C* is a fitting parameter of the dip angle distribution on the input triangulation (STL input file); the effect of direction is included by projection of the true dip of triangles to their apparent dip in the respective direction. Evaluation in SRC is done in 5-degree steps.
- Fractal model parameters – the fractal dimension *D* and the proportionality factor *A*, defined by a power regression $R_q(w) = Aw^H$ of the RMS dependence $R_q(w)$ on the window size *w* [m] (a subarea of the evaluated surface), where the Hurst exponent, *H*=3-*D* (for a planar surface) or *H*=2-*D* (for a line profile), is an alternative expression of *D* used also below (roughness represented by *A* and *H*).

The measures are evaluated for (1) the smaller sub-area of the measured fracture representing the intersection with a borehole core, (2) synthetically generated surfaces on the 200 mm scale, (3) the whole area of the measured fracture (200 mm). The comparison is a part of verification and prediction-outcome exercise.

Synthetic surface generation with upscaling

The fractal model (presented above as a roughness metric) was used to generate synthetic surfaces, using the method implemented in the SRC software. It contains the scaling effects directly in its concept – the dependence of RMS on the spatial scale by the power function. The roughness control parameters of the generator are H (Hurst exponent) and R_q (RMS of the whole required area).

While H is directly a result of the measured surface analysis (smaller-scale sub-area in this task) and is scale-independent, R_q for the target larger scale (upscaling) is obtained by substituting this scale (i.e. the generated surface size, w=200 mm in this task) into the power regression formula $R_q(w) = Aw^H$ (A is available as the second roughness measure of the smaller scale real surface together with H). This is illustrated in Figure 3-1. We note the method is different from the form applied in Task 10.2.1 – that case represented the upscaling with the same slope in a log-log graph (i.e., the Hurst exponent of the power function) but starting from the final point of the measured data (R_q on the whole measured scale) instead of extension of the regression line used here.

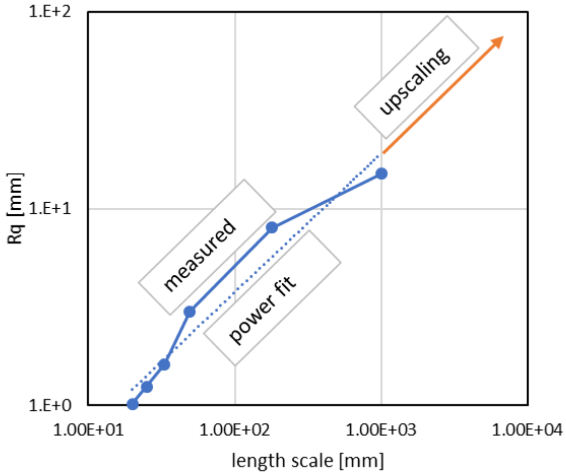

Figure 3-1. *Principle of upscaling with the fractal roughness model parameters.*

In this task, we aimed to define a single roughness parameter set for the generation (all realisations from the same control parameters). The statistical processing of the multiple roughness measures of the small-scale surface variants described above (size, position, and resolution) is part of the prediction-outcome exercise.

Although the fractal surface generation is implemented in SRC, we found a likely bug in the function which is next in the processing sequence: conversion of the generated grid into an STL triangulation, expected as the input format for the analysis. Several large triangles were randomly present but not properly connected to the processed surface. Instead, we used an alternative implementation of the same generation method, available as a user-created MATLAB function: artificial_surf() (Kanafi 2023). The result has been exported with another user function Surf2stl (McDonald 2023), with the only drawback being that it is extremely slow. The algorithms usually require the number of points in one coordinate of the generated grid to be a power of 2.

Aperture calculation

The aperture is needed for the stress-flow model. In principle, synthetic aperture fields could be generated from statistically defined fracture surface roughness, as intended by the task assignment. However, this procedure is theoretically non-trivial because it requires preserving the spatial correlation between two opposing, stochastically generated surfaces. The software available to us did not support such correlated surface generation. Developing and validating a custom implementation would have required substantial effort and time beyond the capacity allocated for this task. Therefore, the measured surfaces of the whole 200 x 200 mm block have been used to obtain a deterministic aperture field, although with uncertainties and free parameters as explained below.

With the aligned grids of the upper and lower surfaces, with 0.1 mm resolution, the aperture field *b(x,y)* was obtained by subtracting the *z* positions of the surfaces $z_{up}(x,y)$ and $z_{lo}(x,y)$. Assuming the coordinate systems of the upper and lower surface scanning are possibly not accurately identical, adjustment displacements in x,y,z directions were considered as

$$b(x,y) = z_{up}(x - x_0, y - y_0) - z_{lo}(x,y) - b_0 \tag{1}$$

where x_0, y_0 are relative shifts in the fracture plane direction and b_0 is the vertical shift, perpendicular to the fracture plane. Their determination is done as part of data preprocessing, b_0 is then finally determined through calibration on the stress-displacement measurements (see subsection below). Considering a fully general position transformation, a relative rotation of the upper/lower surfaces could also be considered, but this was skipped because it was considered technically difficult.

The adjustment in *x,y* direction was done, as in Task 10.2.1, by minimizing the surfaces penetration, which is an optimization problem of minimizing the area with $b(x,y) < 0$ with x_0, y_0 as fitting parameters. This can only work if the surfaces are appropriately close to each other in the z direction, i.e., with a coarse estimate of b_0. For this case, a few line profiles were visualized, and the aperture median (for the original coordinates) was evaluated to be equal to 0.32 mm. The estimate b_0=0.2 mm was chosen, i.e., with surfaces closer to each other than the raw data (Figure 3-2). Then, the optimization for x_0, y_0 (simple search in 0.1 mm steps) minimizing the total contact/penetration area lead to a displacement by 0.1 mm in the positive *y* direction for the upper surface, but visually with a very small effect.

The "negative apertures", $b(x,y) < 0$, are present even after the horizontal position optimization. The respective area (grid elements) is interpreted as the contact between surfaces in an unloaded state. An eventual constraint on b_0, i.e., that the whole area $b(x,y)$ is positive, is not considered realistic – very few points (hypothetical peaks) would require the surfaces to be far from each other. The negative values of *b* are interpreted as measurement inaccuracies or an effect of the surface damage due to the block dismantling. Instead of comparing the contact area with the pressure film image (Task 10.2.1), the effective measured stiffness in normal stress is used to fit the contact area (by means of direct determination of b_0, see below) and the pressure film measurement is considered later for the evaluation of results (section 4.2.1).

For further processing, the aperture values linked to the regular 0.1 mm grid are interpolated to the triangulation used for numerical solution of flow and for evaluation of aperture changes due to normal load – as described in the following subsections.

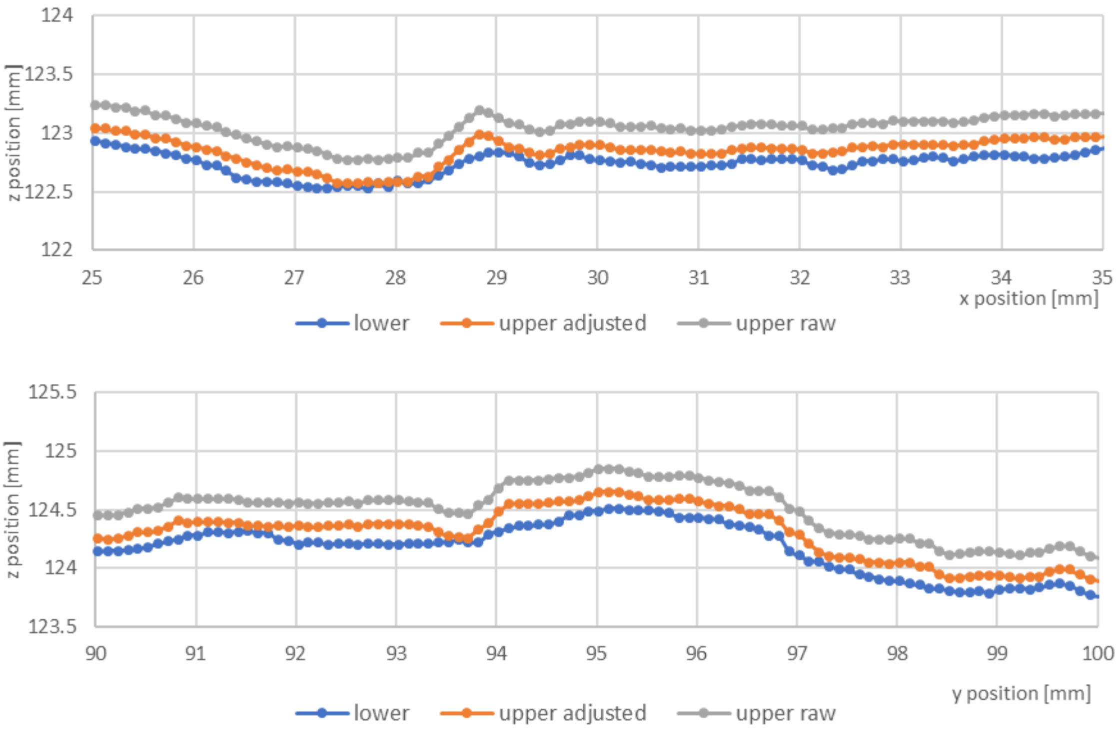

Figure 3-2. *Examples of the fracture surfaces profiles – segments along the x coordinate (position y=0) and along the y coordinate (position x=0). The temporary vertical adjustment b_0=0.2 mm is shown, used for the horizontal adjustment optimization. Mind the same axes scales of both plots. Points show the grid steps (0.1 mm).*

Flow calculation

2D local cubic law in the horizontal plane is considered (Witherspoon et al. 1979, Brush and Thomson 2003, Isakov et al. 2001); the particular application is described below. Flow simulations were only performed for the "measured" aperture field (no aperture fields were generated for the synthetic surfaces). The stress effects are included through stress-dependent aperture fields, as explained in the next subsection.

We consider the horizontal projection of the fracture (*xy* plane) with apertures field *b(x,y)* obtained by subtracting the Z positions of the surfaces, from which local transmissivities for each mesh element (details below) were determined based on the cubic law. Therefore, all data (distances, velocities) are considered as projections to the *xy* plane.

For general non-horizontal fracture surfaces, this simplification overestimates the aperture and the hydraulic gradient: (1) applied aperture calculation expresses the vertical distance while the transmissivity would be controlled by the distance perpendicular to the local surfaces, (2) hydraulic gradients are evaluated in the horizontal projection while the flow would be controlled by the gradient along the surface. These effects depend on a factor of cosine of the surface angle. No such compensation was applied in the reported calculations. Changes of density and viscosity with temperature were neglected (the reported variations seem to be very small).

Flow123d developed at the Technical University of Liberec was used for the flow calculations (Brezina et al. 2020). The GMSH (Geuzaine and Remacle 2009) file formats are used for geometry and transmissivity input. Firstly, a mesh of desired size (".msh" file, GMSH native file format) was created with 0.4 mm resolution – found as the lowest element size reliably working in the solver. Then an input file in the format ".bln" (see the Surfer documentation) containing the mesh points and element centres was prepared in MS Excel and the function Residuals in Surfer was used, projecting the aperture from the grid onto the element centres. Then the data part of the input ".msh" file in MS Excel was designed (according to Flow123d file format documentation) and the transmissivity section was compiled using the local cubic law for individual mesh elements. We note that although the STL triangulation had been already available, it was not suitable for transformation to the Flow123d input, because there was no link to the distribution of the aperture data.

To get a numerically well-posed problem, the aperture and transmissivity fields need to be above a certain positive limit (threshold). A value of 0.001 mm was chosen for the minimum aperture; the corresponding transmissivity is approximately 8×10^{-13} m^2/s. For comparison of the model with flow measurements under large normal stress, after this data was disclosed, also other thresholds were considered. Visualizations of the transmissivity fields are shown in Figure 3-3 for two different adjustments of the vertical positions (b_0 introduced in the previous subsection, values determined below from the mechanical model calibration).

Two configurations of boundary conditions were used to generate X and Y gradients, respectively. Pressure heads of 4.34 m and 0.71 m (reference case of the experiment) were specified across two of the opposite fracture sides, and zero flux for the other two sides. The pressure difference is interpreted as a scaling factor for the linear problem and for comparison with measurements under other pressure gradients, e.g., a transformation to common difference of 1 bar over the cropped sample size of 190 mm has been used.

Stress and deformation model concept and calculation

This model expresses the relation between the applied force on the block and the observed displacement between the sensor mounting points in the experiment. With the one-way coupling between the hydraulic and mechanical problem, the hydraulic pressure is neglected in the stress-displacement evaluation and the resulting aperture field, obtained by postprocessing of the displacement, is used as input to the flow model.

The problem is not suitable for application of a common 3D finite-element elasticity model, leading to too large a problem with the given surface geometry resolution. Although specific approaches can be found in the literature (Tian and Bhushan 1996, Zou et al. 2020, Min et al. 2009, Zangerl et al. 2008), a simple approach was applied, which was easy to implement, to reduce the work and computational time.

We decompose the mutual force action of the upper and lower blocks into a system of independent actions of columns representing variable positions of both fracture surfaces at the discretization elements of the horizontal area, as shown in Figure 3-4 (can be considered for either a triangulation or a uniform rectangular grid). This means that the asperities are evaluated independently of their neighbors. Such columns cover only a part of the block height, h_f, which represents the zone of non-uniform stress. We refer to the Saint-Venant principle, which states that the effect of non-uniform load "disappears" after a distance proportional to the size of the loaded area by a factor of order unity. Here the appropriate scale could be anything between a discretization element and the whole block. The stress is considered uniform on the upper and lower block surfaces. The transition is gradual in reality; therefore, the bound between the columns and the uniform blocks is only conceptual, and therefore h_f is considered to be a free parameter. It will be called "fracture zone" below, but it has not a meaning of rock matrix disturbance, but only a non-uniform stress in the intact rock environment.

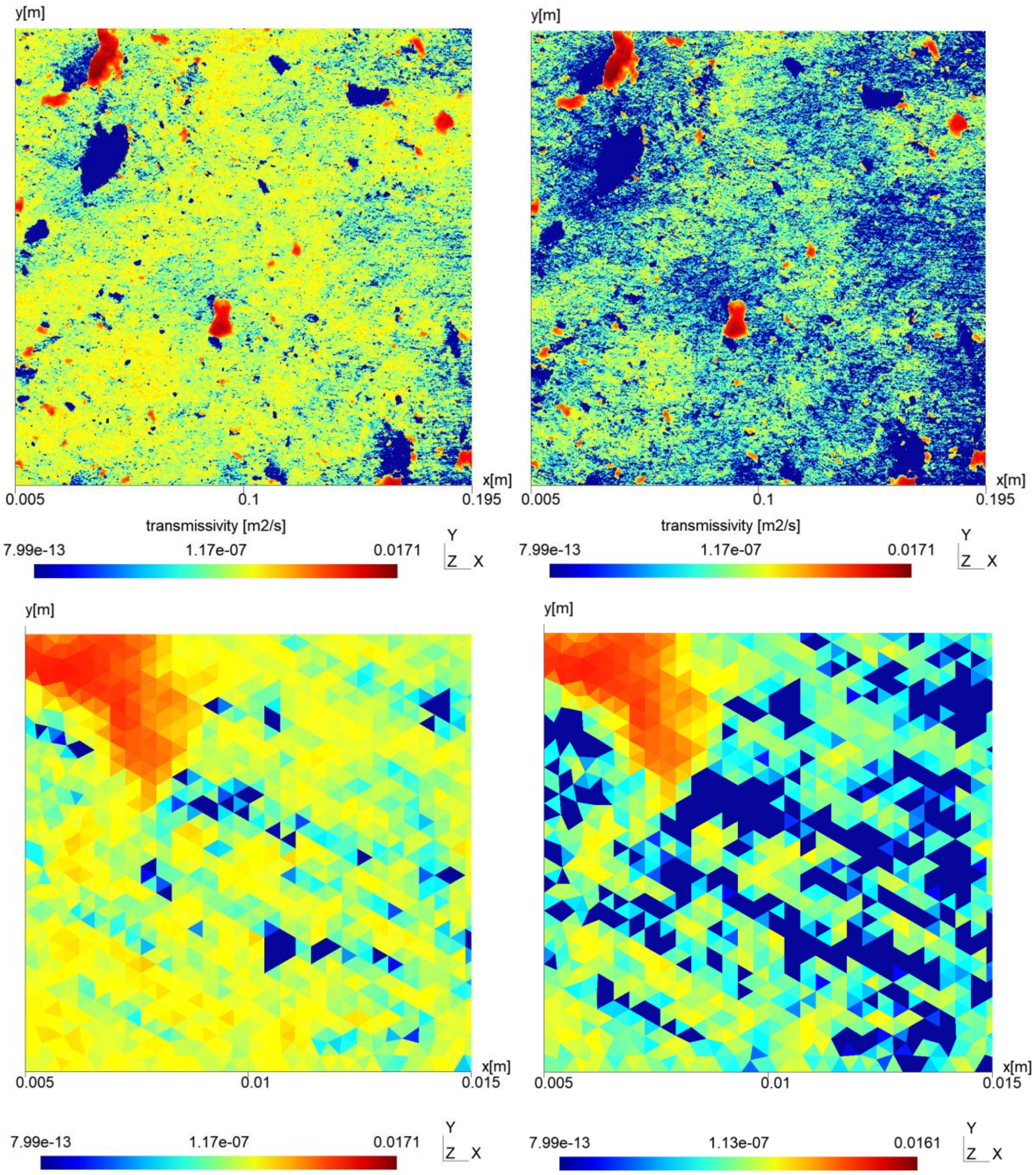

Figure 3-3. *Examples of the discretized fracture aperture fields: upper row is for the full model size; lower row is for a detail (about 5% of the distance) with visible triangular elements. Left column is for the applied vertical shift of* b_0*=0.25 mm, and right column is for* b_0*=0.306 mm (values derived and used below). Logarithmic scale is used.*

This creates N uniaxial stress problems (one for each discretization element, i.e., each column in Figure 3-4). The total force is the sum of the forces corresponding to these partial areas. Depending on the displacement of the columns, contact and compression (and force generation) of particular columns either will or will not occur. It is controlled by the difference between the local initial aperture and the relative displacement of the upper and lower blocks captured by LVDT. We denote ΔS_i the discretization element area (i its index), b_i the aperture of this element (the center point value of the function *b(x,y)* defined above can be both positive and negative), Δh_f the contraction of the fracture zone height, and E the Young's modulus of elasticity. We introduce the symbol for the "positive part of the function", which characterizes the condition whether or not the contact will occur in the given elementary discretization surface:

$$[x]^+ = \begin{cases} x & x > 0 \\ 0 & x \leq 0 \end{cases} \qquad (2)$$

Then the total force on the block can be expressed from the conditional compression of the columns within the fracture zone, depending on the mutual displacement Δh_f of the interfaces between the fracture zone and the stress-uniform parts of the upper and lower blocks (see Figure 3-4), i.e.

$$F\left(\Delta h_f\right) = \sum_i F_i = \sum_i \frac{E\left[\Delta h_f - b_i\right]^{+} \Delta S_i}{h_f} \tag{3}$$

where F_i are forces at the individual elements, which can be either zero (open aperture) or positive (being a compressive force at the contact). It should be noted that an inverse relation will be needed to solve the problem that infers the dependence of the displacement on the applied force (and the consequent change of the aperture field, i.e., the positive part of the opposite subtraction $\left[b_i - \Delta h_f\right]^{+} \geq 0$, i.e., in places without contact). But $F(\Delta h_f)$ is non-linear due to the conditional function for the contacts. It is not possible to write an explicit relationship for the inverse dependency in this case.

For comparison with the LVDT measurement, also the deformation of the respective height of the block parts with uniform stress, below and above the fracture zone, needs to be considered. The total contraction Δh, composed of the fracture zone compression Δh_f discussed above and the compression resulting from uniform stress changes in the block, is given by

$$\Delta h = \Delta h_f + \Delta h_b = \Delta h_f + \frac{F(\Delta h_f)(h - h_f)}{ES} \tag{4}$$

We need to express Δh as function of F. The system is equivalent to a problem of indeterminate stress of two coupled columns (the fracture zone and the uniform-stress block in our case) subjected to the same axial force, where the total elongation/contraction is known, but individual elongations/contractions are unknown. It could be solved by a simple formula if each column were linear elastic (system stiffness equal to the harmonic average of each component stiffness). This is not applicable if the stiffness is nonlinear and only expressed by an implicit formula. Moreover, neither of the calculation directions can be done: $F \rightarrow \Delta h$ or $\Delta h \rightarrow F$. Nevertheless, such functions can be given as a parametric curve: the auxiliary parameter Δh_f must be taken first from a defined range and used for the calculation of both F and Δh, defining finally the desired stiffness relation $\Delta h(F)$. The practical application will be explained below.

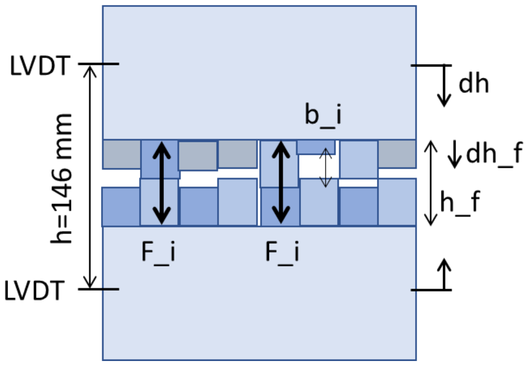

Figure 3-4. *Conceptual model of the stress problem: Inner part is the "fracture zone" affected by non-uniform stress, where columns (index i across all) correspond to the numerical discretisation of surfaces and apertures, with force distributed to contacts. Outer symbols give the relation of quantities to the measured LVDT displacement (shown quantities: $\Delta \boldsymbol{h}$, $\Delta \boldsymbol{h_f}$, $\boldsymbol{h_f}$, $\boldsymbol{b_i}$, $\boldsymbol{F_i}$).*

Stress model calibration

An example of a stiffness calculation is shown in Figure 3-5: The variable Δh_f starts at the minimum of $h(x, y)$ over the whole surface (i.e. a negative number expressing the hypothetical penetration) and it is increased until the force and the displacement remain in the reasonable ranges. $F(\Delta h_f)$ is plotted in blue (calculated directly by equation (3)) and $F(\Delta h)$ is plotted in orange, calculated as the parametric curve (technically by adding the uniform block contraction to the corresponding points of the blue curve, equation (4)). For small stresses, fracture zone deformation dominates (blue and orange curves coincide); for larger stresses, the contribution of uniform-stress matrix deformation becomes significant or even dominant. For lower h_f=5 mm (left plot), a higher force is needed to generate a chosen contraction for the given stiffness and consequently the contribution of the compression of the uniform-stress matrix is higher. The effect is also shown in Figure 3-6: the $F(\Delta h)$ dependencies asymptotically converge to a line with the slope corresponding to the homogeneous block stiffness (all contacts at the fracture become active and the fracture zone gets the same stiffness as the uniform-stress matrix). This is a useful limit for comparison with measured stress-deformation data.

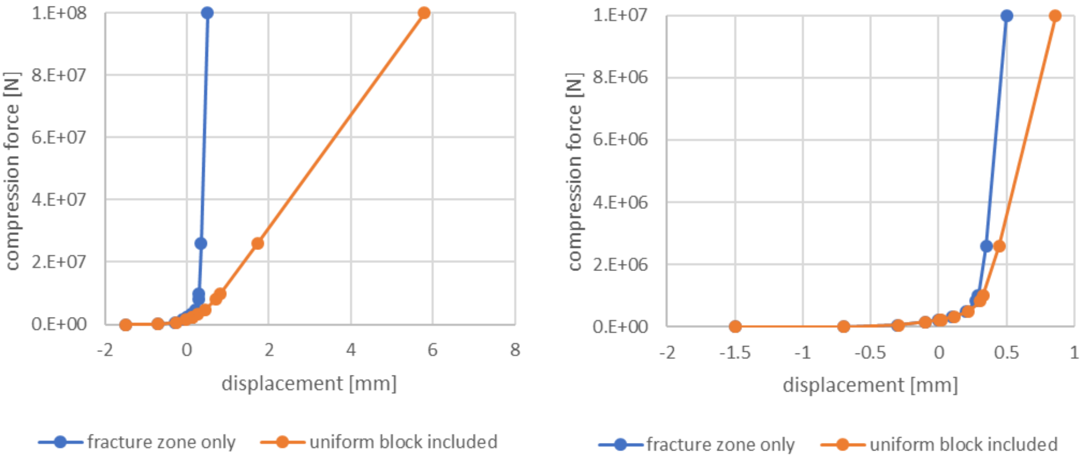

Figure 3-5. *Dependence of force on displacement for the normal fracture compression model. Left for the fracture zone thickness* $\mathbf{h}_f$*=5 mm and right for* $\mathbf{h}_f$*=50 mm.*

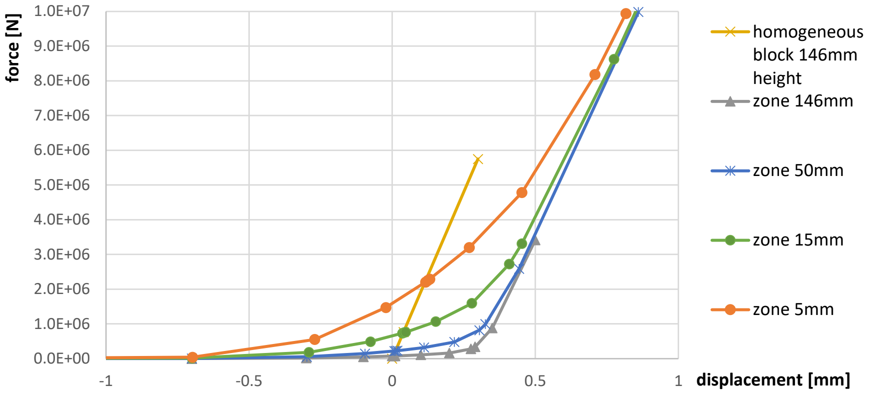

Figure 3-6. *Dependence of force on displacement for the normal fracture compression model for various* $\mathbf{h}_f$ *choice with observation of the asymptotic behaviour as a homogeneous block of intact rock (full fracture contact in the model).*

The following concept of the model calibration comprises two free parameters into a single fitting procedure: (1) the fracture zone thickness h_f (conceptualization only, no data available to support the estimate) and (2) the vertical adjustment of the relative position of the two laser-scanned fracture surfaces b_0. The latter could be supported by other aperture-related data (trace photographs, pressure films) but they are not considered in this procedure.

The idea is shown in Figure 3-7. There is always a nonzero force for zero displacements resulting from the initial surface penetration in the unloaded state (negative values of the subtraction of the raw upper and lower surface position data). Such force is considered as a measurement artefact – an effect of inaccurately mating surfaces. Eventually, the additional displacement b_0 could be applied as an adjustment of the vertical block positioning (coupling of the two laser scan coordinate-systems, see the respective section above), changing also the value of the artefact force. This is interpreted as moving the coordinate origin of the displacement-stress plot along the curves, i.e., the values $F'(\Delta h_f) = F(\Delta h_f) - F(b_0)$ and $\Delta h'(\Delta h_f) = \Delta h(\Delta h_f) - \Delta h(b_0)$ are used as quantities of the model output.

At the same time, we consider the data of the LVDT measurement during loading, which result in an approximately linear slope along quite small intervals of stress and displacement values – this is expressed by the thick black lines in the plot, which should fit the slope of the model stress-displacement curves, if starting at $\Delta h(b_0)$ and $F(b_0)$. For the calibration, there are two free parameters (initial displacement b_0 and the fracture zone thickness h_f) and one fitting constraint of the measured slope (as mentioned in section 2.3.3, this value representing the linear stiffness is extracted from the measured data), leaving one degree of freedom for the parameter choice.

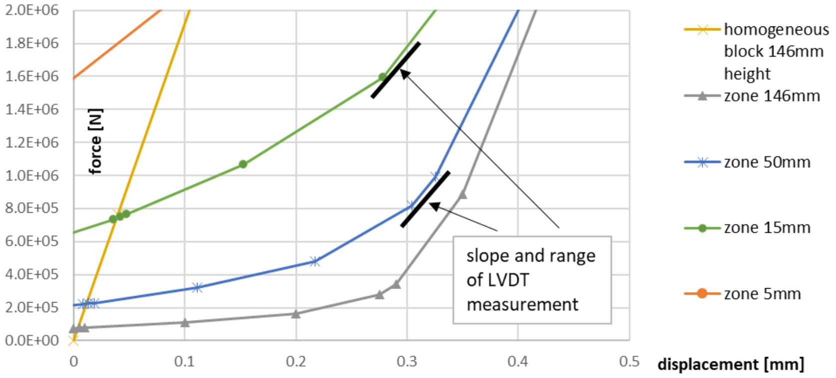

Figure 3-7. *Dependence of force on displacement for the normal fracture compression model for various* h_z *choice. In the lower detail, the linear approximation of LVDT data is attached, considering zero positions of both the force and the displacement are uncertain.*

3.1.3 Determination of critical aspects

Several assumptions were made, which were mainly motivated to get a technically feasible model with enough support from the provided data. They are eventually justified through the prediction-outcome exercise below.

- We do not consider surface changes during block disassembling and reassembling, but their potential effects on measured data and model/measurement comparison is discussed in the text.
- We considered the block fracture edges out of scope of the study. Using the raw scanning data leads to open channels, but there is no such effect on flow, although the type of side sealing is not expected to penetrate into the fracture (rubber block, not liquid or paste). However, this is critical only with respect to a laboratory experiment, not to real fracture, which is not ended this way.
- There is general uncertainty of the mutual upper/lower block position, but only the translation adjustment is applied in the procedure, without a rotation. Some of the pressure film data suggest a non-uniform distribution of stress (one corner is more stressed than others) which could be caused by a position different from the natural state – this is not evaluated in the work, except the final visual comparison below (section 4.2.1). Only the average of the four displacement sensors has been used for the mechanical model calibration and for the aperture change calculation.

- Local cubic law and horizontal fracture place projection is used. The real conditions for flow could be different. Additionally, the results can be sensitive on mesh resolution, which was smaller than the surface data resolution.
- The fractal model is based on infinite scale range, but the data covers only a limited range. It is discussed in the text (Section 4.1.2), how it could affect the relation of measured and synthetic surfaces.

3.1.4 Model parameters

We list all quantities controlling the model from all data sources (directly provided within the task dataset, derived, taken from other sources, or chosen without explicit support).

Processing the geometry

- Grid resolution (0.1 mm used for the whole sample and 0.25 mm for final evaluation of the borehole-scale subarea).
- Distance for the fracture area horizontal cropping (5 mm used).
- Choice of the subarea representing the borehole scale (square sides in the respective section).
- Triangular mesh resolution for stress and flow calculation (0.4 mm used), to which the surface and aperture data is projected.
- Horizontal relative block position adjustment (upper surface by 0.1 mm in y direction).

Synthetic surface generation

- Controlling parameters of the fractal model – target RMS of the whole surface (Rq) and the Hurst exponent H (values determined in the respective section, H=0.888, A=0.0251 mm, derived Rq=2.80 mm).
- Resolution of the generated surface (2048 points along the square side, i.e. about 0.1 mm grid resolution).
- Number of realizations.

Mechanical model

- Initial position adjustment of upper/lower block parts, a choice based on generic expectation of fracture tightness (two variants 0.25 mm and 0.275 mm).
- Height of the non-uniform stress zone (fracture zone) – fitted parameter to get a desired stiffness depending on the above parameter of initial position (27 mm and 65 mm respectively).
- Vertical block distance covered by the LVDT sensors (146 mm).
- Horizontal area of the cropped surfaces (36100 mm2).
- Intact matrix Young modulus (70 GPa).

Flow model

- Aperture field (derived from the geometry data).
- Choice of minimum aperture value in the places of contact (0.001 m in the prediction, adjusted with the validation data).
- Mesh resolution for numerical discretisation (0.4 mm).
- Hydraulic pressure boundary conditions (given by measurement, but small variations neglected by a choice of 3.6 m hydraulic difference and other gradients represented by the model linearity).

3.1.5 Identification of influential factors

The influential factors affecting the results were identified based on exploratory model runs and practical experience with the model behaviour rather than through a formal sensitivity analysis. Some are already listed in section 3.1.3. A factor was considered influential if its variation led to noticeable changes in the main model outputs. Quantitative factors are

- Mesh/grid resolution: for source surface data, roughness calculation and generation, flow model solution
- Size and shape of the area used for small-scale surface roughness analysis
- Choice of one of the parameters (a degree of freedom for the prediction) in the mechanical stress-displacement model, the initial displacement
- Choice of temporary z adjustment for the x,y adjustment optimization
- Non-linearity of the flow (flow rate not proportional to pressure gradient, but without observable fracture closure/opening)

3.1.6 Workflow describing the modelling process

The workflow roughly follows the organization of the nonnumbered subsections of 3.1.2, but there are actually two separate branches for the rough surface upscaling and for the hydromechanical test prediction. This is a consequence of the synthetic aperture field (correlated surfaces) not being done in the work.

Common

1. Point cloud kriging to grid 200 mm [resolution choice, consistent with source data accuracy/resolution].
2. Cropping the grid (edges exclusion) [decision, amount choice].
3. Multiple subareas repeated kriging to more resolution grids [software tools limitation, decision to evaluate more variants, choice of resolution, size].

Surface generation branch

1. Evaluate roughness measures for the whole fracture (this would not be necessary at first, but due to many technical difficulties and software bugs, it was useful to check if the evaluation works properly).
2. Take subareas, evaluate roughness measures, do statistics, decide on synthetic generation control [number of synthetic control variants, complexity of statistic – here intentionally the simplest choice, repeats 10.2.1., no depending task].
3. Generate the surfaces as grids [choice of number of realisations, resolution].
4. Transform into a triangulated mesh.
5. Evaluate roughness measures for synthetic surfaces.
6. Evaluate the results (e.g. compare the small-scale and large-scale roughness measures, individual realisations).

Hydro-mechanical modelling branch

1. Generate the geometry and discretisation (triangulation in our case) for the numerical model of flow.
2. Evaluate a reference aperture field, projected to the triangulation.
3. Estimate the initial relative position correction of the two surfaces (x,y,z).
4. Calibrate the mechanical model, i.e., fit the slope of the stress-displacement dependence, by combined choice of vertical position correction b_0 and the fracture zone width h_z.

5. Evaluate the set of aperture fields for various loads.
6. Run the flow simulation with the respective aperture input.
7. Compare the simulation results with measurements and update the mechanical model calibration parameters if needed.

3.1.7 Pragmatic validation aspects

In Table 3-1, we summarise explanations of the points defined in Section 2.4.

Table 3-1. Pragmatic validation aspects – reference or explanation for the workflow points in Section 2.4.

Order	Description	Solution/reference
1	Model purpose	Section 3.1.1. Based on the task definition, additional focusing.
2	Domain of applicability	Facts of model limitation mentioned in several places.
3	Critical aspects	Section 3.1.3
4	Performance measures and criteria	Section 3.2.1 and 3.3.1. Quantities defined based on the task description. Participation of the evaluator expected.
5	Conceptual assumptions tested	Assumptions in general as part of Sections 2.3 and 3.1.2. Measured data confirmed that the surface has fractal features (power regression possible). The simplified stress distribution around the fracture adequately represents the larger-scale hydraulic phenomena.
6	Derivation of numerical parameters	Described in Sections 3.1.2, 3.2.2, 3.3.2. The choice of fractal model parameters verified against their large-scale surface counterparts. The choice of fracture zone (non-uniform stress) confirmed by the non-linear stiffness evolution. The choice of the initial displacement of surfaces confirmed by the resulting fracture transmissivity.
7	Scope and limitation of experimental data	Not done systematically. Some important cases discussed in detail in the respective sections: range of scales to be captured by the fractal model power regression, uncertainty of the reference “zero” of the displacement sensors, irreversible changes of the fracture surface, flow not proportional to pressure gradient.
8	Sensitivity and uncertainty analysis.	Not done systematically and formally. In some cases there are model variants evaluated in parallel and compared.
9	Prediction-outcome exercises	Sections 3.2.2, 3.3.2. The predictions of synthetic upscaled surfaces could be compared to one coupled upper/lower measured surface of the intended size, but not as a blind prediction. The stress-displacement relation was extrapolated to larger range than the known data for calibration and to the state of the block after opening. The flow rate prediction could be compared to direct measurements. Both extra stress-displacement data and all flow rates were predicted blindly.

Order	Description	Solution/reference
10	Evaluation, documetation, audit	As a continuation of prediction-outcome section, the evaluation is done in Section 4 and discussed in more generic context in 5.1. As per the task definition, further participation of the evaluator is considered.
11	Pragmatic validation statements	This step is only addressed here in a preliminary and self-evaluative sense. A full formulation of pragmatic validation statements requires synthesis across multiple modelling teams and approaches, and therefore lies beyond the scope of this single-team modelling report.

3.2 Prediction and validation of the upscaled fracture geometry

3.2.1 Definition of performance measures and criteria

The performance measures are the quantities describing the surface roughness. We use

- Fractal model parameters (RMS for the whole surface)
- Directional roughness metric

The concept of the performance measure evaluation is that the calculated measure of the generated large-scale surface is compared with the corresponding measure of the (smaller-scale) surface used as an input for the generator of synthetic fracture surfaces.

3.2.2 Task 10.2.2a: Prediction-outcome exercise of the upscaled fracture geometry based on an artificially constructed core sample

First, the roughness was analysed for the smaller-scale area (borehole equivalent, in the form of sub-squares). The fractal parameters were evaluated, which were needed for the synthetic surface generation. The fractal dimension D and the proportionality factor A are plotted in Figure 3-8 for variants of the smaller area selection and discretisation. The point cloud is irregular but there is a clear trend related to the discretisation (Figure 3-8 right). Considering the finer discretisation more accurate in general, the average of all sub-square variants with 0.025 mm resolution was used as one pair of A and D for the generation (shown as “average fine”). The distribution of points could eventually suggest selecting two representative points for the subsets lower left and upper right on the plot, but it was not of interest for the other parts of this work. We did not observe systematic differences between the lower and the upper surface.

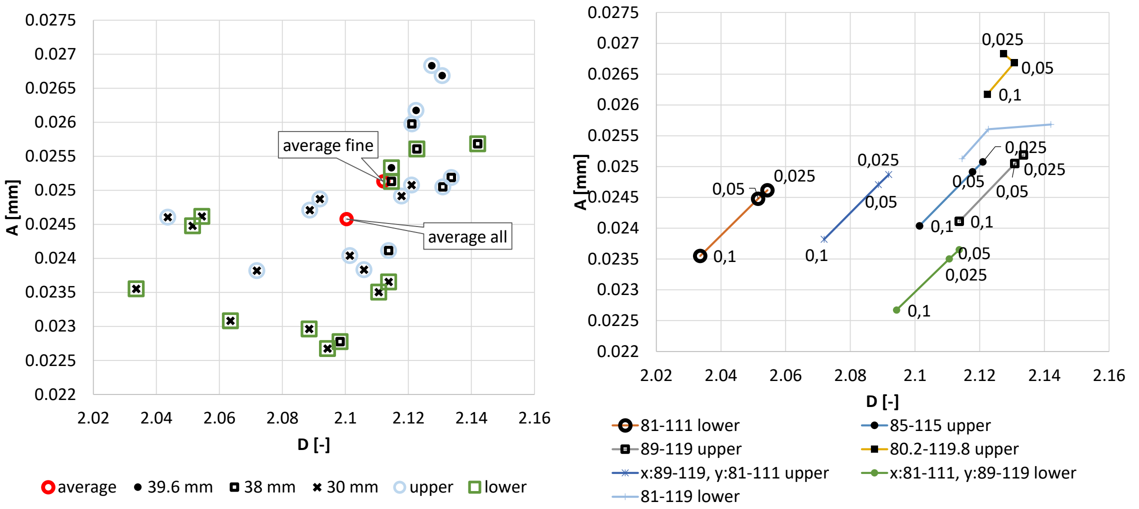

***Figure 3-8.** Roughness measures of the subareas of the fracture surfaces corresponding to a borehole – parameters D and A of the fractal model. Effect of size and upper/lower surface is emphasized on the left, and effect of discretisation (values in mm) is emphasized on the right (cases of the same surface area are connected).*

Ten synthetic surfaces of 200 x 200 mm size were generated. To verify the upscaling concept and calculation, the roughness measures of the synthetic surfaces are planned to be compared with the roughness measures of the measured upper and lower surfaces of the 200 x 200 mm real fracture, see the results in Section 4.1.1 below.

3.3 Prediction and validation of flow along a fracture at different normal loads

3.3.1 Definition of the performance measures and criteria

Based on the task assignment and the experiment concept, the main performance measure is the value of flow rate (depending on the applied normal stress). At the moment of prediction, a deviation from linearity of the pressure gradient and the flow rate was not considered, so that the set of more tests with different gradients under the same normal load are considered as multiple measurements of one quantity (transmissivity), expressing uncertainty.

Additionally, as the linear representation of the stress-displacement (LVDT) measurement on the limited stress range was only used for the model calibration (slope – constant stiffness), the actual non-linearity of this dependence and its extrapolation to higher stresses can be considered as a performance measure. We should note that these results were not published within the Task Force group before the validation data disclosure, but there were no changes of the model made after the blind prediction of the 320 kN state, and the same methodology was applied for intermediate and higher load step evaluations.

3.3.2 Task 10.2.2c: Prediction-outcome exercise of flow along an unopened fracture at different normal loads

Before the prediction, the model is calibrated to the stress-displacement measurements as described in Section 3.1.2. It includes an additional parameter choice – the initial displacement b_0. Then, the deformed aperture fields are evaluated for a given loading step and input to the flow calculation model (Section 3.1.2) after the minimum positive aperture adjustment. The resulting flow rates for the initial and final load states (320 kN) are evaluated. Although not affected by the validation data disclosure, the mechanical and hydraulic model results for the intermediate loads and higher loads were evaluated later and are presented below in Section 4.2 (but would be normally a part of the prediction if the procedure was used in the full extent).

Two choices of the initial displacement were made: 0.25 mm and 0.275 mm, placed in the transition zone of the displacement-force curves from low to high stiffness and representing a reasonably closed fracture (with respect to the aperture median of 0.32 mm of the raw surface coordinate data – unadjusted coordinates).

Then the displacement change Δh_f in the loaded state was iteratively changed together with the fracture zone thickness h_f until both the applied force ($F'(\Delta h_f)$=320 kN) and the measured LVDT displacements ($\Delta h'(\Delta h_f)$=0.04 mm) were fitted (this is a unique solution with two conditions and two unknowns, considering a single fixed b_0). Technically, it was made by the Excel Solver function. The results are shown in Table 3-2. For the purpose of the predictive model, only the initial and final state of loading were evaluated. We note that the model predicts the force-displacement relation close to linear as was the measurement in the rising load sequence. As mentioned above in the model description, there is only a coarse fit for technical reasons.

The calculated flow rates for the prescribed hydraulic gradient according to the experiment documentation (heads of 4.34 m and 0.71 m) are plotted in Figure 3-9. As mentioned above, only the initial and final load is evaluated due to limited time until the data disclosure. The difference between the two variants is very large, one to two orders of magnitude. The effect of normal stress on the flow rate is of similar magnitude. We note that, by coincidence, the loaded deformation of the second variant is almost equal to the initial deformation of the first variant. These cases consequently lead to the same flow rate (same aperture field). The choice of the variant (65 mm/0.275 mm or 27 mm/0.25 mm or any other consistent in a one-parametric set) represents the uncertainty of the prediction. However, the choice defines points on one hypothetical curve of the displacement-flow rate relation but linked to different stresses (depending on a variant of the stress-deformation model).

In Figure 3-10, plots of pressure field and velocity fields are shown (three cases of displacements as commented above).

Table 3-2. Fitted model dimensions and deformation parameters and results (the two columns are two equally valid predictions, the first row is an assumption, and the last row is the value fitted to the LVDT measurement).

Quantity	var.1 value	var.2 value
Initial displacement (no force) b_0 [mm] – choice	0.275	0.25
Fracture zone thickness h_f [mm] – result of calibration	65	27
Final fracture zone displacement (loaded) Δh_f [mm] – fitted input to the parametric function	0.3067	0.276
Fracture zone contraction [mm]	0.0317	0.026
Uniform block contraction [mm]	0.0093	0.0135
Total contraction [mm]	0.0409	0.0395

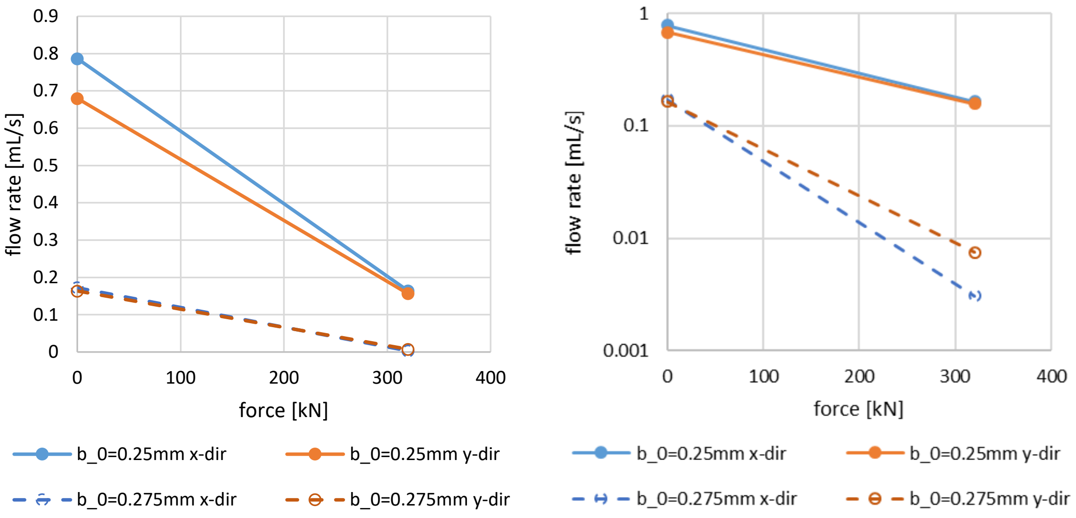

Figure 3-9. *Results of the hydromechanical model – dependence of flow rate on the compressive force, for two variants of different initial vertical displacements (of no force) and two hydraulic gradient directions, linear (left) and logarithmic (right) flow rate axis.*

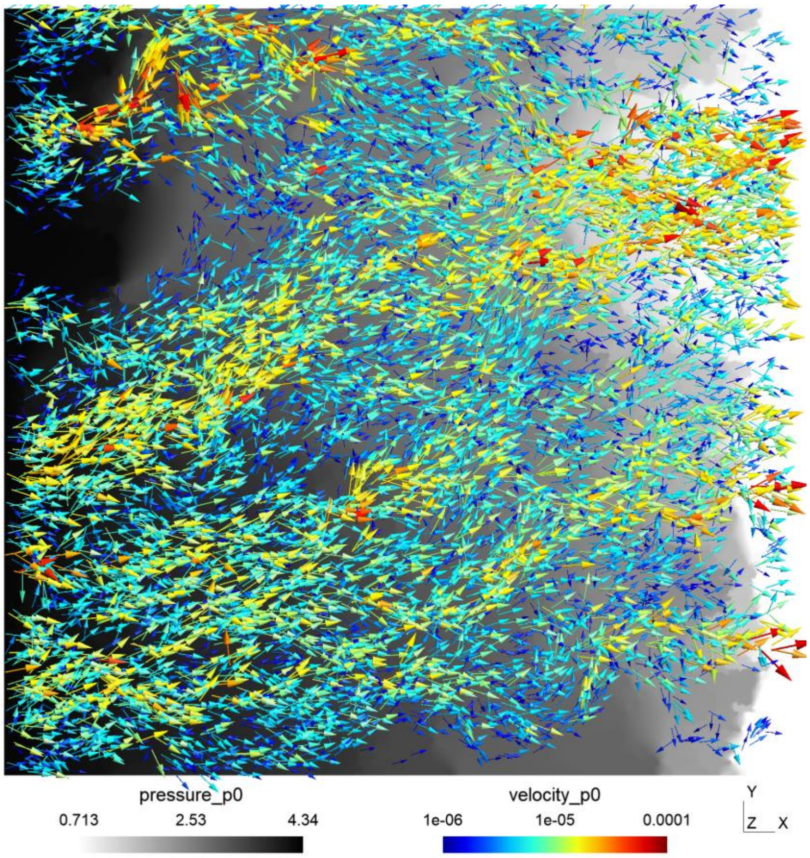

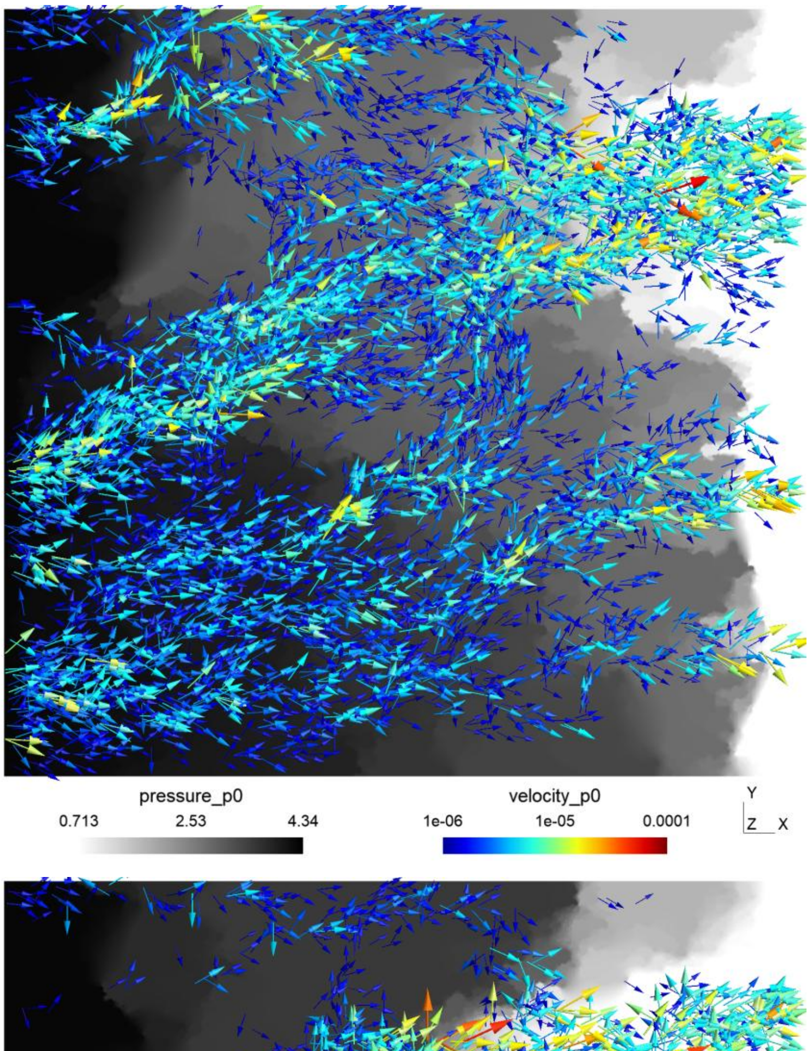

Figure 3-10. *Results of pressure head [m] and velocity vectors [m/s] (arrows, log scale for length and colour, lower limit, every 40th symbol shown) for the three fracture zone displacements: top 0.25 mm (initial of the second case), middle 0.275 mm (final of the second and initial of the first case), bottom 0.306 mm (final of the first), see Table 3-2.*

4 Results

The results are presented in two subsections, corresponding to the two solved prediction-outcome exercises, i.e., Task 3.2 – fracture geometry upscaling – and Task 3.3 – stress-dependent flow.

4.1 Fracture geometry upscaling

4.1.1 Comparison of generated and measured surfaces

The roughness measures of the synthetic surfaces, made as predictions in Section 3.2.2, were compared with the roughness measures of the measured upper and lower surfaces of the 200 x 200 mm real fracture. The comparison of the fractal model parameters is shown in Figure 4-1, including the smaller-scale data used as generation control input. The circles correspond to the data in Figure 3-8, so the larger-scale roughness parameters are significantly off the "cloud" used as source data for generation – in other words, the uncertainty of the upscaling and of the synthetic generation is larger than the uncertainty in the smaller-scale area selection and analysis procedure. Besides that, the parameters of the synthetic larger-scale surfaces are also substantially different from the corresponding measured sample.

When looking on the directional roughness metric (Figure 4-2), the fit is good concerning the magnitude of the metric, but the anisotropy is not well captured (the generated surfaces were controlled as isotropic), although the relative differences are small.

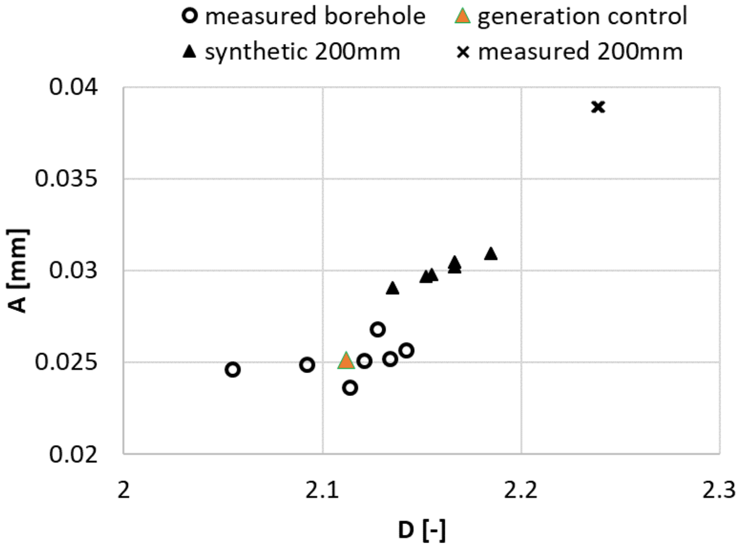

__Figure 4-1.__ Fractal model parameters as the roughness measures compared for the borehole scale (used as the input for the generation) and 200 mm scale, and between the synthetic and the real surfaces. The synthetic 200 mm scale differs from the generation control and from the measured surface on the corresponding scale.

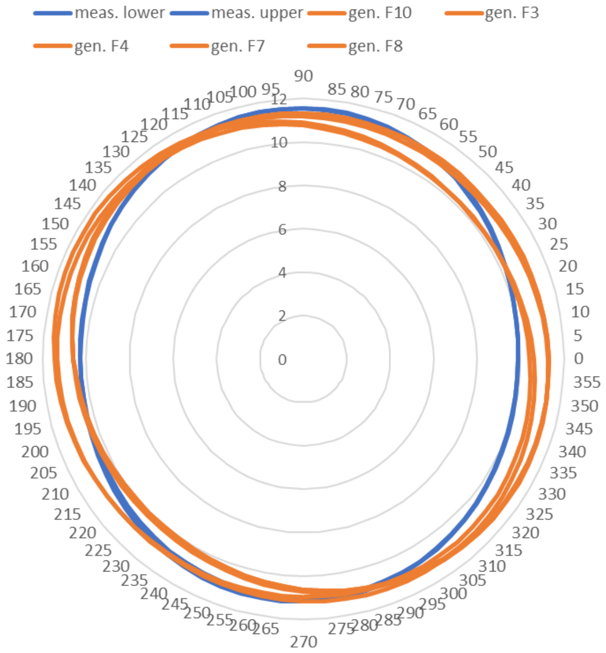

Figure 4-2. *Comparison of the directional roughness metric between the individual synthetic realisations (predictions) and the two real surfaces of the same scale of 200 mm (upper and lower with almost the same values).*

4.1.2 Evaluation of differences

While the fit of the directional roughness metric was quite good between the predicted 200 mm surfaces and the measured 200 mm upper and lower surfaces, there was a large difference between parameter pairs H and A determining the fractal roughness, all between the small-scale measured, larger-scale measured, and large-scale predicted fracture surfaces (Figure 4-1).

Figure 4-3 suggests an explanation for the fractal roughness measures misfit. Regression lines in the log-log plot of $R_q(w)$ power dependences are plotted for several smaller-scale measured surfaces (blue), several synthetic 200 mm scale surfaces (orange) and the measured 200 mm surface (the upper and lower surfaces are actually expressed by almost the same line). The problem can be seen as a generic uncertainty of extrapolation: the lines form a relatively narrow strip in the middle, but they diverge for very large and very small scales. Consequently, the slopes and intercepts can be significantly different, although the lines are not so far from each other in a certain data range, in the middle of the captured scales.

This consideration could also be extended with an evaluation of the data accuracy used for the regression. The fractal model assumes the relation over an infinite scale range, which is not achievable for real data. There are other roughness models using a term "truncated power function". In practice, the largest and smallest-scale data could be seen as less reliable: At the largest scale, only a single realisation is available (the entire surface), so this endpoint is sensitive to the particular surface selection and provides no within-scale statistics. The small-scale data is limited by grid resolution (surface subareas need to cover a representative number of grid steps to evaluate the RMS statistics) – a size close to the grid size is evaluated with more uncertainty.

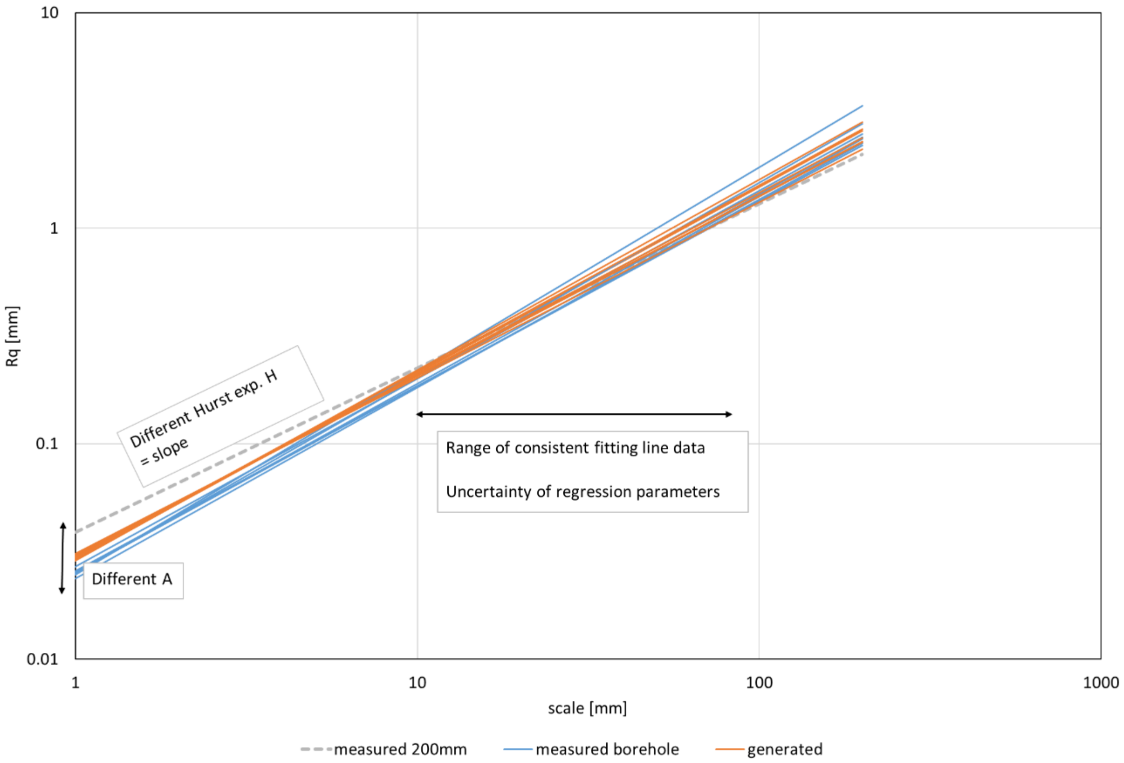

Figure 4-3. *Regression lines expressing the power dependence of the fractal roughness model. Data for several individual subareas of the measured surface ("borehole", multiple blue lines), synthetic realisations (multiple orange lines) and the whole measured fracture (upper and lower surfaces visually coincide, grey dashed line).*

As a resulting interpretation, the divergence of the regression lines in Figure 4-3 (and therefore the spread of the data in Figure 4-1) can be affected by inaccurate data points at the ends of the regression intervals. Therefore, the misfit between the model output data (synthetic large scale) and the measured data (small scale for input and large scale the same as of the synthetic), if present mainly at the ends of the regression intervals, is not considered critical argument against the model validation. Additionally, this evaluation can be considered as a basis to determine the "application range" of the model.

4.2 Fracture flow simulation under normal stress

In this section, we primarily evaluate the measured data in the context of the model blind prediction and some extension calculations. This tightly follows the insights gained from the prediction-outcome exercise.

From the two calculated prediction variants, the choice with h_f =65 mm and b_0 =0.275 mm, i.e., the larger displacement representing the relative adjustment in the vertical coordinate of the upper and lower surfaces, and the smaller resulting flow rate, was used for the comparison with the measurement – considering it fits the disclosed flow measurement by an order of magnitude better than the second variant. In addition to the cases with zero and 320 kN force used for calibration in Section 3.3.2, all the intermediate load steps (40, 80, 160 kN) were calculated with the same meaning as that of the blind prediction, although formally obtained after the flow data disclosure.

Concerning the measured values, there were sequential steps of variable hydraulic gradient, which could potentially lead to a different transmissivity interpretation (i.e., non-linear pressure-flow rate dependence). The prediction model was based on the local cubic law and therefore linear in this context and does not allow to explain the source of nonlinearities. Neither the effect of the hydraulic pressure to the stress/deformation model or damage effects from opening and resealing the fracture were considered. Therefore, all the hydraulic gradients are considered equivalent; to make the comparison, all the flow rates were transformed (normalized) to the hydraulic difference of 1 bar over the fracture length, including the model results (i.e. the presented values in figures differ from section 3.3.2, where the measured heads were used directly).

The comparison is plotted in Figure 4-4 and Figure 4-5 for the respective two gradient directions. The x direction (1-3 direction) was measured for the unopened fracture only, with the normal force increased up to 320 kN. There is about one order of magnitude difference in flow rate, which decreases systematically with increasing force, indicating convergence between the model predictions and the measurements. The changes in flux caused by an increase in load of the measurement are clearly smaller than the model/measurement differences. The situation is similar for the y direction (2-4) and the unopened fracture case, both qualitatively and quantitatively, except the smaller model/measurement difference for the unloaded case.

For the resealed fracture, the normalised flow dataset shows a markedly larger scatter than in the unopened-fracture case discussed above; the data does not collapse onto a single curve, indicating a nonlinear (non-Darcy) relation between gradient and flow rate. Next, higher flow rates were measured for the "unloaded" case (1 kN). This can be explained as settling of the sample, re-fitting of the two fracture surfaces. The (gradient-normalized) measured flow rate deviation is of the similar magnitude as the prediction/measurement difference. The model result falls near the boundary of the measurement envelope (scatter), attributed to nonlinear hydraulic and assembly/disassembly effects.

Practically, the case after reassembling and resealing can be considered more relevant to the model (laser scanning captures the state after opening the fracture, i.e., the real initial state for the resealed experiment), while the unopened case would be closer to the natural state of the fracture. Such phenomena introduce a bias when upscaling from small-scale laboratory characterisation data to the large-scale predictions.

After the comparison of the prediction model, the calculation was done for the larger applied normal forces, 800 kN and 1500 kN. The resulting flow rates are included in Figure 4-5, together with the predictions. The flow rates are significantly smaller than the measurement and against the model for smaller normal stresses. The slope for the model data decreases more quickly than for the experimental data. In this case, it was necessary to check the effect of the minimum aperture threshold, applied for numerical reasons (to avoid fully impermeable elements at contacts). The theoretical flow rate by the cubic law for the uniform aperture of such a threshold is shown in the plot. It is likely that the flow rate for the most loaded case is mainly controlled by the threshold value. Therefore, the calculation was repeated with a choice of 0.5 mm, instead of 1 mm. The flow rate decreases about the same factor of 8 as for the uniform case. The concave curve resulting from the mechanical model asymptotically approaches the flow rate of the fracture with uniform minimum aperture.

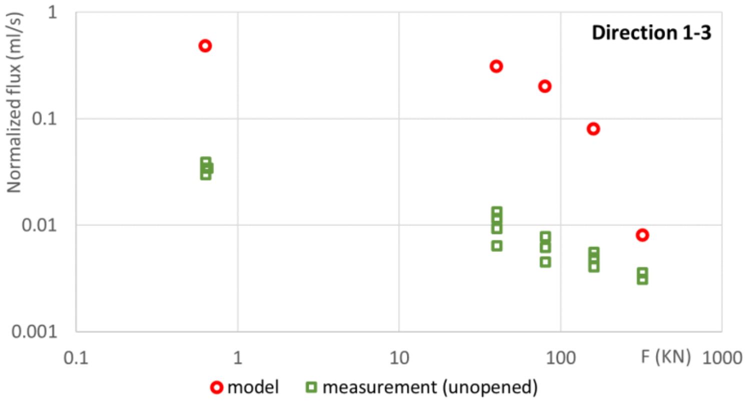

Figure 4-4. *Comparison of the predictive model with the measurement of the flow rate through a fracture depending on mechanical load in the normal direction (the direction 1-3 refers to the task definition, corresponding to the x direction).*

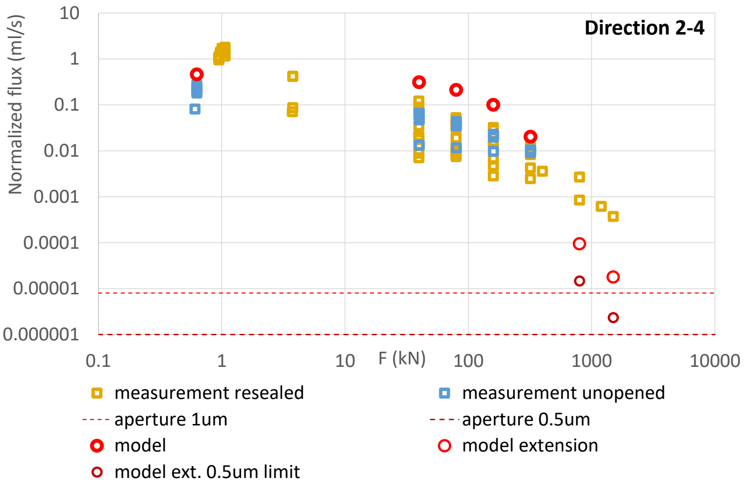

Figure 4-5. *Comparison of the model with the measurement of the flow rate through a fracture depending on mechanical load in the normal direction (the direction 2-4 refers to the task definition, corresponding to the y direction). The thick circles denote the predictive case and the thin circles the results calculated after the measurement disclosure. Dashed lines show the cubic-law flow rate for uniform aperture (two cases in the legend).*

Next, we evaluate the mechanical model itself on extended data, i.e., the features of the measured stress-displacement curve, which were not used for the model definition and calibration. The measured data in the later disclosed package includes the stress-displacement measurement on the opened and resealed block. In Figure 4-6, the new data is shown together with the measurement on the unopened block in the limited force range to focus on the behaviour in the range of the initially available data (0–320 kN force range). There is a significant shift of the measured displacements, so the plots are made with two independent axes but with the same range. The upper and lower limits of loading/unloading cycles correspond to the loading and unloading cycle of the unopened block, except the interval between zero and the lowest force of 40 kN. The resealed block data indicates much smaller stiffness in this interval, which can be explained as settling of the mechanically disturbed surfaces which do not mate precisely. This can also explain the need for a relative shift of the displacements to compensate for the relatively large displacement during this initial fracture surfaces settling.

The comparison of the measured stress-displacement curves with the model predictions is shown in Figure 4-7 and Figure 4-8. The two model variants determined by the fracture zone width and the initial displacement have very similar results and can therefore be evaluated together. The first plot contains the range of the data available for the prediction model input (although only the linear approximation was actually used in our case). The concave shape is very close to linear and corresponds with the measured curve of the loading direction. The second plot focuses on the behaviour under large loads (here the whole range of the measurements is shown in contrast to Figure 4-6; moreover, a single vertical axis is used, so that the shift in the raw data is visible). Except for forces under 80 kN, the pattern of nonlinearity (slightly concave shape) is consistent between the model and the measurements. The effect of settling of the inaccurately mating surfaces (early part of the curve) is conceptually the same phenomenon, which is intentionally excluded by definition of the zero force for the displacement b_0, which is understood as the adjustment of the coordinate system. In Figure 3-7, the “excluded” part is everything below and to the left of the thick black lines, which represent the effective model range. Note that the plots here (Figure 4-6, Figure 4-7 and Figure 4-8) have opposite meaning of the horizontal and vertical axes than Figure 3-7; the actual value ranges and slopes do not correspond between the unadjusted model (Figure 3-7) and the transition between the 0–80 kN and the rest of the measured force-displacement curve on the resealed block.

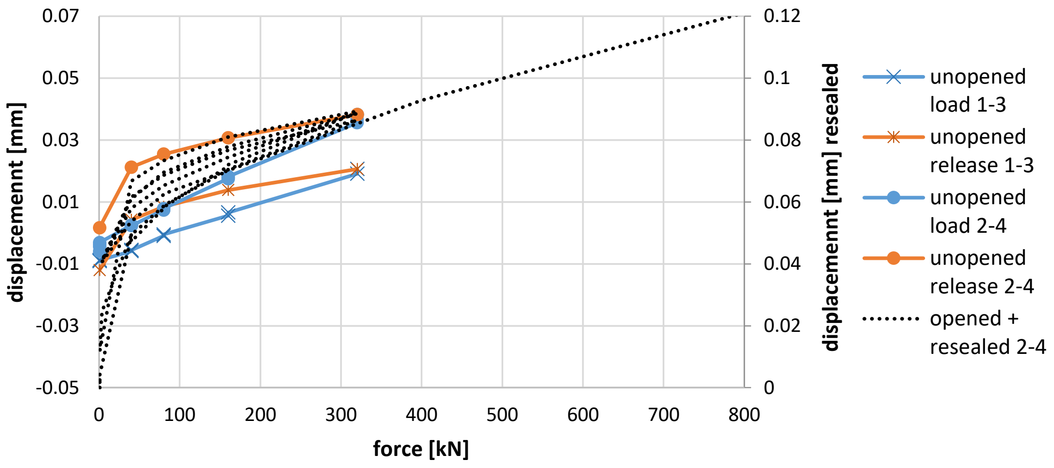

Figure 4-6. *Comparison of the stress-deformation data of the unopened block available for prediction and of the resealed block including higher stresses, which was disclosed later for validation. The load/unload cycles are not distinguished in the resealed case. The axis for the resealed case is shifted but of the same scale.*

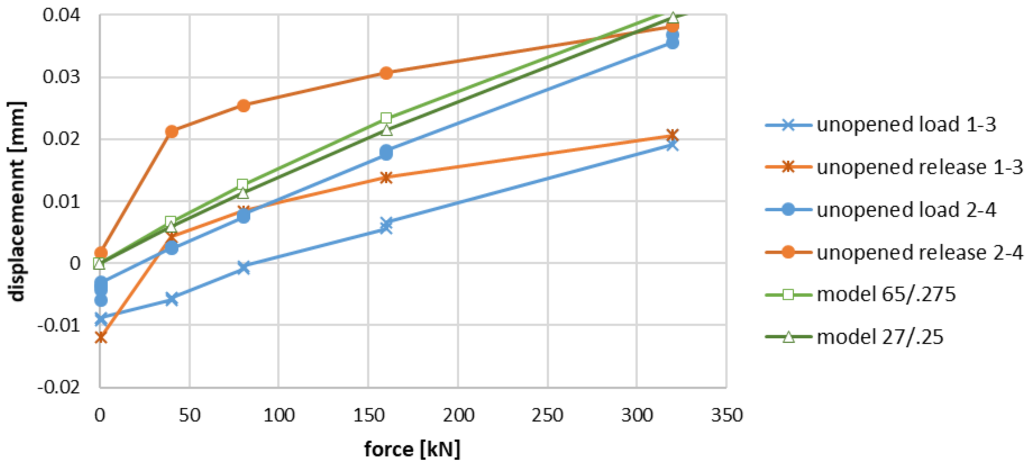

Figure 4-7. *Comparison of the model stress-deformation data (two variants defined in the text) against the experiment on the unopened block. Slightly concave shape of the two model curves should be of interest.*

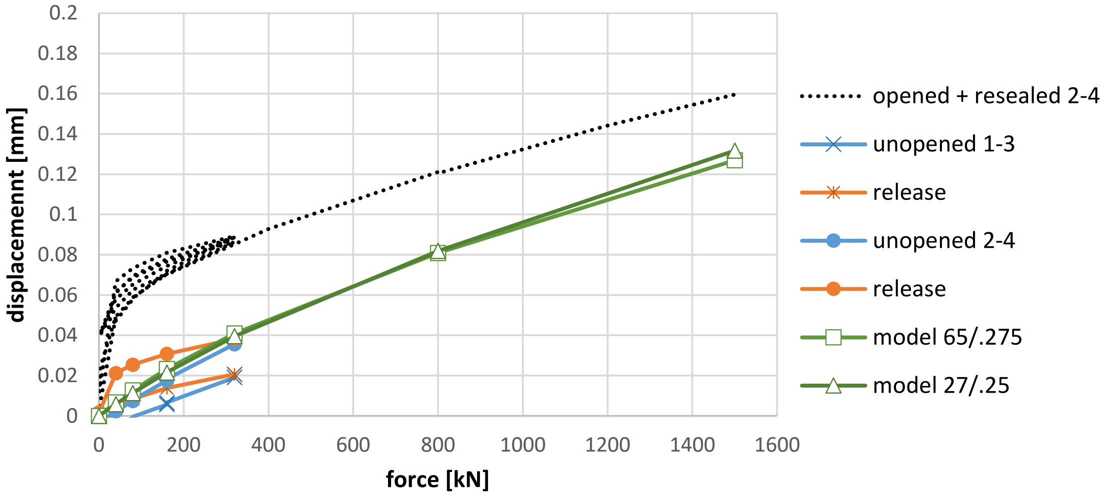

Figure 4-8. *Comparison of the model stress-deformation data (two variants defined in the text) against the experiment on the opened and resealed block, with higher range of applied stresses. Note the common vertical axis in contrast to Figure 4-6.*

4.2.1 Pressure film evaluation

The pressure film measurements were not used as a direct input to the flow simulations and do not form a primary part of the quantitative validation of the hydro-mechanical model. Instead, they are employed as a complementary and qualitative consistency check of the mechanically derived aperture fields, and hence of the realism of the predicted contact area distribution under normal loading. In this sense, the pressure film data support the pragmatic validation framework by providing an independent observational constraint on the spatial pattern of fracture contacts.

The comparison presented here is purely qualitative. A quantitative interpretation of the pressure film images was not feasible. Previous attempts to derive absolute contact stresses from the digitized pressure film images were not successful. The manufacturer-provided colour scale was coarse, and integration of pixel-wise values did not reproduce the applied normal force. In addition, the digitization of the original colour images (pink-scale tones) introduces further uncertainties that may accumulate spatially.

Figure 4-9 compares the model-predicted, stress-dependent contact area distribution with the contact patterns inferred from two types of pressure films ("MS" and "LW", see the Task Description), each for two different applied normal pressures 1 MPa and 4 MPa. The source pressure film images were not spatially referenced to the laser scanning coordinate system; therefore, no geometric scale is shown and only qualitative spatial patterns are compared. Colours represent relative magnitudes of contact pressure, but the absolute values are not meaningful in this context and are therefore not shown.

In the model visualisation, the grey areas represent contacts in the reference (nominally unloaded) configuration after correction of the mutual block position based on the mechanical calibration (Section 3.3.2, Table 3-2, variant 1). The coloured overlays indicate additional contact areas activated under applied normal loads. Specifically, the reference state corresponds to a relative vertical shift of 0.275 mm, the load of 1 MPa (40 kN) to an additional displacement of 0.0055 mm (total 0.2805 mm), and the load of 4 MPa (160 kN) to an additional displacement of 0.0186 mm (total 0.2936 mm).

The two types of pressure films (MS and LW) exhibit markedly different spatial patterns, even at a qualitative level. This already indicates significant sensitivity of the measured contact patterns to the pressure range of the film, and possibly to the film thickness and stiffness. Such differences point to potential measurement artefacts and limit the interpretability of the data. Furthermore, parts of the fracture surface were damaged during block handling and opening. The laser scanning captures asperities that were later partly removed; consequently, some areas predicted by the model as contact correspond to no contact on the pressure film images. Conversely, larger cavities in the modelled aperture field (clearly open areas) are consistently reflected as non-contact regions in the pressure film. This comparison thus also serves as a qualitative check of the reference (unloaded) configuration rather than of the load effect alone.

At the scale of several centimetres, the global spatial patterns show partial consistency between the model and the measurements: regions with pronounced contact and regions with sparse or no contact tend to coincide. However, a systematic quantitative relationship between different areas is not reproduced. For example, the pressure film images show a pronounced gradient from lower contact intensity in the upper-left part of the images to higher contact intensity in the lower-right part, which is not captured by the model. This suggests a possible rotational component of block deformation during loading that is not represented in the presented mechanical model.

At finer spatial scales (individual discretisation elements or film pixels), the patterns differ substantially. The pressure film typically shows contact domains with characteristic sizes of millimetres to centimetres, whereas the modelled contact distribution derived from the laser-scanned surfaces appears more "speckled", reflecting the high-frequency roughness of the scanned geometry. This discrepancy indicates that either the model overemphasises small-scale roughness effects, or that the pressure film response smooths the contact distribution due to its finite thickness and mechanical properties.

Overall, the pressure film comparison provides a qualitative plausibility check of the spatial organisation of fracture contacts and their evolution with normal load. However, due to the combined effects of measurement and data processing artefacts, the pressure film data appear not suitable for quantitative calibration or validation of the applied mechanical or hydraulic models.

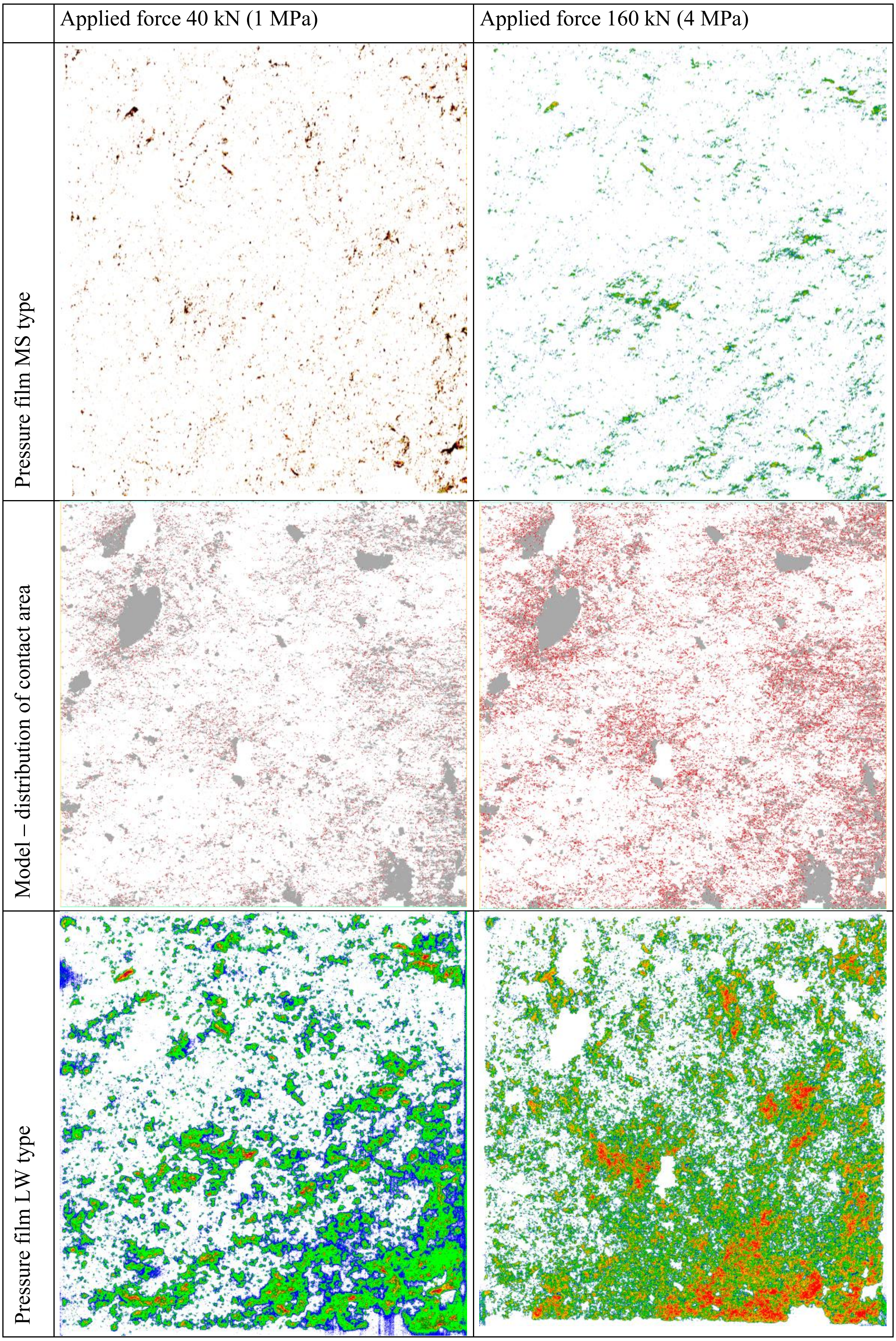

Figure 4-9. *Comparison of the model stress-dependent contact area distribution (middle row) with the measured contact data by means of pressure film (two types, top and bottom row), for two different loads (columns). The source pressure film was not referenced to coordinates, so no scale is shown. Colours represent magnitudes of pressure – the values have no meaning for this comparison, therefore the colour scale is not included.*

5 Discussion, summary, and conclusions

5.1 Discussion

The goals of the pragmatic validation exercises were achieved, although some parts of the defined Task 10.2.2 were missing, in particular the synthetic generation of apertures, i.e., of two correlated rough surfaces. Although it had not been formulated as an explicit goal, but not using all available data (either for input or for validation) means that the implicit goal of the modelling was not fully achieved. Nevertheless, capturing all process details was not the goal, so neglecting the fracture irreversible changes, the stress-strain hysteresis, or coupled hydraulic-mechanical effects, does not mean that the goals of pragmatic validation were missed. A detailed sensitivity analysis was not formulated as a goal but it is missing as part of the pragmatic validation. In line with the Task 10 concept, pragmatic validation statements are primarily intended to be formulated at the level of cross-team synthesis and evaluator-led assessment, rather than within a single modelling contribution.

The ideas for improvements partly follow the mentioned missing features. Potentially, the following details could be included: variable transmissivity with fluid pressure, fit of the pressure-displacement nonlinearity curves, and incorporation of mutual block-part rotation (for both the initial alignment adjustment and the representation of the stress effect, i.e. including moment equilibrium). The pressure film data would, in principle, be well suited to support the calibration or validation of an extended stress–deformation model including block rotation, as the observed contact patterns visually indicate large-scale non-uniform loading. In practice, their quantitative use was hindered by measurement artefacts.

The next point of discussion is regarding the appropriateness of the provided data. The difficulty with the data is not the amount or the resolution, but the fact that modelled processes and properties are sometimes hidden by other effects, including a "noise" which is difficult to interpret as a physical phenomenon with quantitative data (effects of dismantling, shift of the stress-strain curve, flow non-linearity). Some of the data may require special knowledge or software tools (e.g., determination of fracture geometry from photographs). Combination of more independent sources of measured data is found to be useful to constrain the model as much as possible and provide the validation – if not used, it is a problem of the modeller, not of the assignment.

The resolution becomes limiting for the small-scale surfaces if the fractal model is based on the scale dependence regression; a large difference between the sample size and the resolution is preferable for statistical reasons. On the other hand, the same resolution can become limiting for large blocks, due to the limited memory capacity and computing power.

Not including the pressure films in the model development and/or calibration represents a different approach from the procedure used in Task 10.2.1 for the adjustment of the upper/lower block positions (Finsterle et al. 2024). The difference is that, for Task 10.2.1, the pressure film is the only source of information on the fracture contact area (i.e., for determining the vertical block adjustments, to achieve partial surface contacts), while for Task 10.2.2, the mechanical stiffness is also available as a measure of the tightness of the contact. In fact, we found the stiffness data more reliable, with relatively accurate sensors of force and displacement (except setting the reference state – "zero displacement"), while in the pressure film, the determination of the contact area can be affected by large errors, although it is in principle a direct measurement, while the stiffness is an indirect measure.

The assumptions, justifications, and uncertainties in the model can be summarised as follows:

- The fracture surface was cropped by 5 mm from all sides for all calculations, and the corresponding difference in the model extent was consistently reflected in the derived quantities. This does not limit the practical applicability of the methodology; a more systematic assessment of scale effects related to the choice of cropped area could be addressed in future work.
- Only three translational degrees of freedom were considered for the mutual positions of the upper and lower parts. Accounting for the substantial differences of the displacement among the four corners can be important to capture the realistic distribution of the aperture, but it was difficult to reliably determine the real displacement with the provided data.

- The effect of the fracture surface damage during dismantling together with generic laser scanning inaccuracy was excluded by selecting a suitable zero point on the modelled stress-displacement curve. It should be evaluated how the model fits the hydromechanical experiment with either the original or the damaged surface state.
- The flow model is based on the local cubic law in the horizontal projection (variable aperture assigned to planar surface). The effect of this simplification is difficult to evaluate without creating a more complex model (e.g., 3D Stokes flow, and approach pursued by other participants of Task 10.2.2).
- Temperature effects are neglected. However, within the reported range, they are expected to be insignificant.
- Effects of water pressure on fracture deformation are neglected. This was made because of technical feasibility, but it could be of interest to verify their potential effect in low applied force steps.

5.2 Summary

Two separate prediction-outcome problems related to each other were solved, both based on common geometric data of a single natural fracture at laboratory scale.

The first problem and model consider the upscaling from smaller area geometric surface data used for model setup (evaluation of roughness measures, input for synthetic generation) to the generation (i.e., prediction) of larger surfaces. For validation, roughness measures of the generated surface were compared to the surface roughness measured on the same, larger scale. In this case, some discrepancies exist in the numerical values of the fractal roughness model parameters, but upon closer inspection of the regression of the scale-RMS dependence, the surfaces were found to be consistent and the deviations were caused by uncertainties in the smallest and largest spatial scales involved.

The second validation exercise involved a numerical simulation of the hydro-mechanical problem, with deterministic laser scanning data of the fracture surfaces of the particular tested block. The coupling is one-directional, i.e., the mechanical model provides as output the deformed aperture field, which is then used as input to the flow model. The mechanical model is based on a conceptual simplification in which the zone of non-uniform stress at the fracture is represented by a set of vertical uniaxial-stress elastic columns, joined to a uniformly stressed remainder of the block across a conceptual (not explicitly defined) boundary. This approach results in a non-linear contact problem with the load on the individual columns that are attached to horizontal numerical discretization elements, depending on the displacements of the fracture surfaces. The model was calibrated on the slope (constant stiffness) of the dependence of the LVDT displacements between the two blocks on the applied force. Only the uniform displacement calculated as the average of the four sensors is considered. The flow is modelled based on the local cubic law in a horizontal plane, derived from the stress-dependent non-uniform aperture field.

There were two predictions, based on guessed values of two free parameters, which determine the added initial displacement corresponding to the unloaded state (block position adjustment). Only one of them, i.e. that with the lower flow rate (expected to be more realistic), was used for the comparison of the blind model prediction with the later disclosed flow rate data and stress-displacement measurements of the resealed block. The predicted flow rates were about one order of magnitude higher than the experimental data. The trends of the dependence of flow on the applied load were quite well captured. Moreover, the shape of the stress-displacement curve of the resealed block was very well captured by the model, except the short range under small load, explained as an effect of irregularities from dismantling and sample manipulation. Even the significantly simplified model of the local stress distribution at the fracture surface contacts can provide results which capture the generic hydromechanical behaviour reasonably well. Nevertheless, the validity of the model at very high stresses is limited, as the model predicts substantially greater fracture closure than was measured.

The validation would be more challenging if performed using the upscaled surfaces, i.e., if the 200 x 200 mm surface data was not known but had to be inferred from small-scale measurements and the proposed upscaling method. Having the measured fracture surface available as the input substantially facilitated the organization of the work, as the synthetic surface generation could be treated independently of the development of the hydromechanical model. This separation made it easier to identify and resolve issues in the roughness metrics and generation algorithms—whether arising from theoretical assumptions, data processing, or software bugs—without propagating errors or delays through a coupled workflow.

We also note that several abandoned work directions and unsuccessful modelling methods were not included in this report to keep it concise and clearly structured.

5.3 Conclusions

The problem required to adopt or develop methods which were not previously used by the authors. Therefore, a significant part of the effort was used to resolve technical issues with the models and methods, instead of fully focusing on exercising the concepts of the pragmatic validation. Many solution decisions were controlled by available software tools, professional experience, and needed effort. Despite considerable learnings and developments, the generation of synthetic aperture fields, which connect the characterisation data and mechanical loadings to the flow predictions of interest, was not achieved.

Each of the two solved validation problems/models – the roughness measures predicted with synthetic generation for fracture surfaces, and the fracture hydromechanical behaviour – lead to results which could be valuable for fracture flow and transport modelling in the repository development programmes. The limitations of the modelling methods were identified and more accurately described. In both cases, the comparison of the predictive model and the measurement was possible (including the blind prediction of data reflecting the mechanical and hydraulic behaviour of a single fracture).

Following the concepts and requirements of the pragmatic validation approach, the task changed the thinking of authors during the usual workflow of modelling, sorting data, formulation of a conceptual model, setting up all inputs to the numerical model, calculations, and evaluation. In the technical chapters, an effort was made to record and explain the model choices and assumptions.

In hindsight, the modelling team would approach the task slightly differently, as follows: At the beginning, define the total time available for the task (pragmatically guided by the ultimate goal of the model for which it must be validated), and strictly spend about a half of that time on the technical modelling work. The second half should be spent on a careful, pragmatic model validation, only spending time on model improvements if the validation acceptance criteria are not met.

References

SKB's (Svensk Kärnbränslehantering AB) publications can be found at www.skb.com/publications. SKBdoc documents will be submitted upon request to document@skb.se.

Březina J, Stebel J, Flanderka D, Exner P, Hybš J, 2020. Flow123d version 3.0.4, available from: https://flow123d.github.io (accessed January 10, 2023).

Brush, David J, and Neil R Thomson. 2003. Fluid Flow in Synthetic Rough-Walled Fractures: Navier-Stokes, Stokes, and Local Cubic Law Simulations: Fluid Flow in Rough-Walled Fractures'. Water Resources Research 39 (4). https://doi.org/10.1029/2002WR001346.

Finsterle S, Hokr M, Balvín A, Jankovec J, Gvoždík L, Hyman J, Viswanathan H, Sweeney M, Wang T-T, Chen P-K, Tu C-H, Choi S, Choi C-S, Lee Y-K, Park K-W, Ji S-H, Stock B, Frampton A, 2024. Evaluation and modelling report of Task 10.2.1 - Geometric evaluation and prediction of fracture surfaces and aperture distributions. Task 10 of SKB Task Force GWFTS - Validation approaches for groundwater flow and transport modelling with discrete features. SKB TR-23-23, Svensk Kärnbränslehantering AB.

Geuzaine C, Remacle J-F, 2009. Gmsh: A 3-D finite element mesh generator with built-in pre- and post-processing facilities. International Journal for Numerical Methods in Engineering, 79(11), 1309–1331. https://doi.org/10.1002/nme.2579

Golden Software, 2023. Surfer, available from: https://www.goldensoftware.com/products/surfer/ (accessed January 10, 2023).

Isakov E, Ogilvie S R, Taylor C W, Glover P W J, 2001. Fluid Flow through Rough Fractures in Rocks I: High Resolution Aperture Determinations. Earth and Planetary Science Letters 191 (3–4): 267–82. https://doi.org/10.1016/S0012-821X(01)00424-1.

Lanyon G W, Davy P, Dershowitz W S, Finsterle S, Gylling B, Hyman J D, Neretnieks I, Uchida M, 2021. Pragmatic Validation Approach for Geomechanics, Flow, and Transport Models in Fractured Rock Masses. Paper (DFNE 21-2369) presented at the 3rd International Discrete Fracture Network Engineering Conference, Virtual, June 2021.

Lanyon G W, Davy P, Dershowitz B, Finsterle S, Gylling B, Hyman J, Neretnieks I, Uchida M, 2024. White Paper essays on model validation. Task 10 of SKB Task Force GWFTS - Validation approaches for groundwater flow and transport modelling with discrete features. SKB TR-22-04, Svensk Kärnbränslehantering AB.

Kanafi M M, 2023. Surface generator: artificial randomly rough surfaces (https://www.mathworks.com/matlabcentral/fileexchange/60817-surface-generator-artificial-randomly-rough-surfaces), MATLAB Central File Exchange. Retrieved May 31, 2023.

Magsipoc E, Zhao Q, Grasselli G, 2020. 2D and 3D Roughness Characterization. Rock Mechanics and Rock Engineering 53 (3): 1495–1519. https://doi.org/10.1007/s00603-019-01977-4.

McDonald B, 2023. surf2stl (https://www.mathworks.com/matlabcentral/fileexchange/4512-surf2stl), MATLAB Central File Exchange. Retrieved May 31, 2023.

Min K, Rutqvist J, Elsworth D, 2009. Chemically and Mechanically Mediated Influences on the Transport and Mechanical Characteristics of Rock Fractures'. International Journal of Rock Mechanics and Mining Sciences 46 (1): 80–89. https://doi.org/10.1016/j.ijrmms.2008.04.002.

Tian X, Bhushan B, 1996. A Numerical Three-Dimensional Model for the Contact of Rough Surfaces by Variational Principle. Journal of Tribology 118, 33–42. https://doi.org/10.1115/1.2837089

Witherspoon P A, Wang J S Y, Iwai K, Gale J E, 1979. Validity of Cubic Law for Fluid Flow in a Deformable Rock Fracture. Technical Information Report No. 23. LBL-9557. Lawrence Berkeley National Lab. (LBNL), Berkeley, CA (United States). https://doi.org/10.2172/5704312.

Zangerl C, Evans K F, Eberhardt E, Loew S, 2008. Normal Stiffness of Fractures in Granitic Rock: A Compilation of Laboratory and in-Situ Experiments. International Journal of Rock Mechanics and Mining Sciences 45 (8): 1500–1507. https://doi.org/10.1016/j.ijrmms.2008.02.001.

Zou L, Li B, Mo Y, Cvetkovic V, 2020. A High-Resolution Contact Analysis of Rough-Walled Crystalline Rock Fractures Subject to Normal Stress. Rock Mechanics and Rock Engineering 53,2141–2155. https://doi.org/10.1007/s00603-019-02034-w